Final Report

Improved Ion Resistance for III-V Photocathodes in High Current Guns

Saxet Surface Science

Contract DE-SC0002268

Gregory A. Mulhollan, Principal Investigator
Key Personnel: John Bierman, Duane Smith
Subcontracting agency: SLAC National Accelerator Laboratory
SLAC personnel: Steven Sun, Piero Pianetta
and Robert Kirby, subcontracting to SLAC

DOE SBIR Program Area: Office of Nuclear Physics
Program Manager: Manouchehr Farkhondeh
Topic: 46d-Particle Beam Sources and Techniques

Phase II Period of Performance
08/15/10 – 08/14/12

Executive Summary

The two photocathode test systems were modified, baked and recommissioned. The first system was dedicated to ion studies and the second to electron stimulated recovery (ESR) work. The demonstration system for the electron beam rejuvenation was set up, tested and demonstrated to one of the SSRL team (Dr. Kirby) during a site visit. The requisite subsystems were transferred to SSRL, installed and photoemission studies conducted on activated surfaces following electron beam exposure. Little surface chemistry change was detected in the photoemission spectra following the ESR process. The yield mapping system for the ion (and later, the electron beam rejuvenation) studies was implemented and use made routine. Ion species and flux measurements were performed for H, He, Ne, Ar, Kr and Xe ions at energies of 0.5, 1.0 and 2.0 kV. Gas induced photoyield measurements followed each ion exposure measurement. These data permit the extraction of photoyield induced change per ion (by species) at the measured energies. Electron beam induced rejuvenation was first demonstrated in the second chamber with primary electron beam energy and dependency investigations following. A Hiden quadrupole mass spectrometer for the electron stimulated desorption (ESD) measurements was procured. The UHV test systems needed for subsequent measurements were configured, baked, commissioned and utilized for their intended purposes. Measurements characterizing the desorption products from the ESD process and secondary electron (SE) yield at the surfaces of negative electron affinity GaAs photocathodes have been performed. One US Utility Patent was granted covering the ESR process.

Task Results Summary

Task 1: Modification of first cathode test chamber for ion studies

The system was successfully modified to incorporate a commercial ion gun into the photocathode test volume. Ion beam shapes and currents were able to be acquired using a beam profile arm added at the same time. The system was used for the task 7 measurements.

Task 2: Set up electron gun in training and interface test system

The small photocathode test system (formerly 'imager' system) was configured, baked and used to train personnel on the ESR technique. It was not transferred in whole to SSRL at the request of the involved personnel, i.e., the program went straight to the photoemission measurements utilizing transferred subsystems.

Task 3: Interface acquisition subsystems into SSRL acquisition system

The existing DAQ system at SSRL was employed in the photoemission measurements during the ESR process.

Task 4: Design chamber modifications for electron stimulated recovery studies

The second photocathode test system was modified to add two electron guns and a beam profiler. It was recommissioned and used in task 8 measurements.

Task 5: Set up and conduct at SSRL electron beam recovery measurements

The photoemission measurements on ESR photocathode surfaces were conducted. The chemical changes at the surface, as seen by core level photoemission, were small, but consistent with the data from task 10.

Task 6: Yield map setup

Dual mapping setups were created so that the systems could operate in parallel rather than share the drive systems. The second system was assembled from a very inexpensive galvanometer system and utilized the same DAQ software as developed for the first scanning setup.

Task 7: Ion species and flux measurements

Ion dosing data were acquired for bulk GaAs (monitored at 633 nm) and 100 nm thick MBE grown GaAs (monitored at 846 nm) for Cs and Cs+Li activated surfaces, with each ion exposure followed by CO_2 induced decay measurements. Data were taken for the following ions: H, He, Ne, Ar, Kr and Xe at energies of 0.5, 1.0 and 2.0 kV.

Task 8: Electron stimulated recovery current and energy measurements

Measurements were performed as a function of electron gun energy and beam current on the ESR process. The low energy LEED electron gun in the fourth system was used to measure the secondary electron yield as a function of energy for activated GaAs.

Task 9: Acquire ESD dedicated quadrupole mass analyzer and prep chamber

A dedicated turn-key ESD 300 AMU range quadrupole mass analyzer was acquired from Hiden Analytical Inc. A flange to accommodate the analyzer and an *in situ* electron gun source was

designed and fabricated. The third system was set up, baked, commissioned and used for task 10.

Task 10: ESD measurements of electron stimulated photocathodes

Ion emission measurements during the ESR process were performed using the Hiden IDP quadrupole analyzer. Positive ions corresponding to activation and absorbate chemicals were detected from the CO_2 photoyield reduced surface. Data from the as–activated surface only showed an activation gas signal during electron beam stimulation.

Products and technology transfer activities

Results were presented at:

The program objectives and results to date were presented at the DOE Nuclear Physics Exchange Meeting, Gaithersburg, MD, October 24-25, 2011.

The Phase I results were published in:

G. A. Mulhollan and J. C. Bierman, "Photoyield Recovery of Cs+NF_3 Activated Negative Electron Affinity GaAs Photoemitters without Additional Alkali Deposition", *J. Vac. Sci. Technol. B* **28,** 899 (2010).

A US Patent was granted:

US 8,298,029, entitled "Method for Resurrecting Negative Electron Affinity Photocathodes after Exposure to an Oxidizing Gas" was issued by the United State Patent office on October 30, 2012.

Paper in progress:

A paper for Phys. Rev. ST Accel. Beams detailing the results of the ion species effects is in progress.

Task 1: Modification of first cathode test chamber for ion studies

The first Saxet photocathode test chamber was modified by Saxet personnel in several ways. A new top flange was designed and fabricated to accommodate the RBD Instruments 2kV ion gun (500 eV - 2.0 kV), a phosphor screen, sample-access viewport and four sets of alkali sources. A cross section of the flange appears below in figure 1. A top view is also provided in the same figure. Due to the sample proximity requirement of the ion gun, the viewport had to be moved from its standard, centered position to ~16° off-normal and off-center. The ion gun is mounted on a large-bore port aligner to allow positioning of the ion beam on the sample. The phosphor screen is on a rotary feedthrough which allows it to be swung into position over the sample location. It can also function as a crude beam knife edge profiler in a subtractive sense with current measured on the sample, although it is not intended to be used in this fashion. The screen is only usable at elevated pressures of sputter gas (~$5x10^{-5}$ Torr).

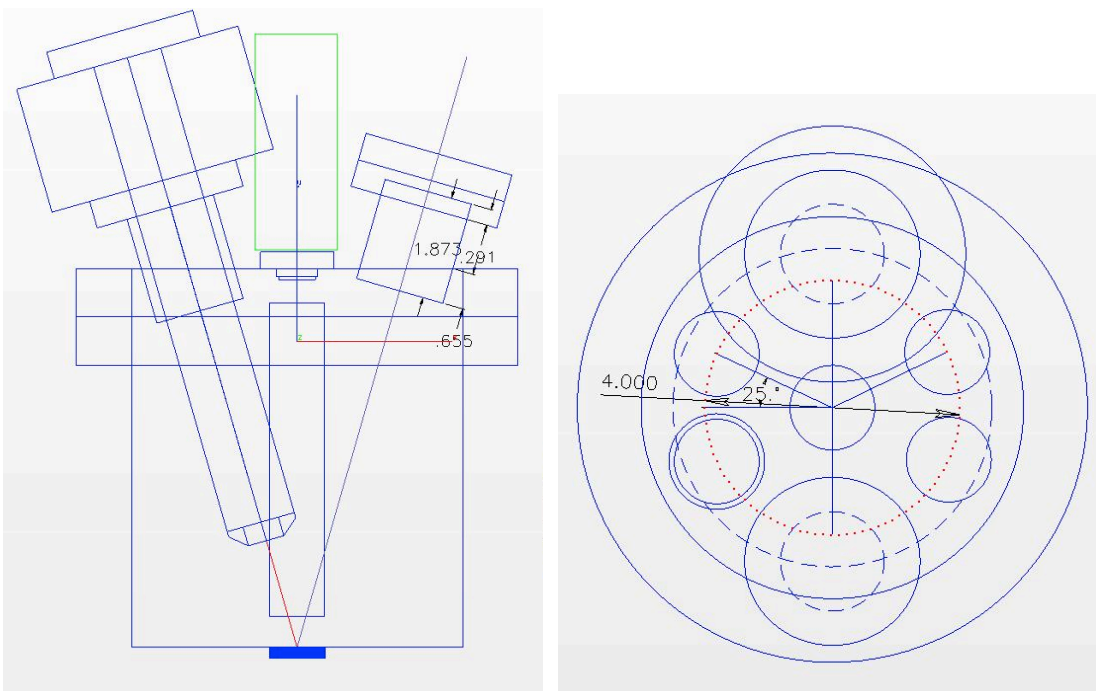

Figure 1. Cross section of new top flange (left) and top view (right). This flange accommodates the ion gun and port aligner (upper left, left drawing), viewport (upper right, left drawing), phosphor arm and alkali feedthroughs.

The installed top flange is shown below in figure 3. Alignment of the ion gun was performed prior to putting the system in bake. The beam is somewhat difficult to see due to the reflected white light from the ionization filament. At 2 kV beam energy with a total pressure of $3x10^{-5}$ Torr (mostly argon), the beam was positioned in line with the gun-viewport axis and positioned approximately 1/3 into the sample from the edge (figure 2). This provides a well-defined region of ion interaction with lesser reacted regions representing the background gas effects (or none in best case). The quantum yield map from the different areas is used to separate out the two different effects.

The alkali sources (two each of Cs and Li) on the top flange were positioned to minimize

deposition upon each other and the ion gun. Other system upgrades included swapping all leak valves for rebuilt units (rebuilding performed in house) and plumbing for activation, noble and decay accelerant gasses. The noble gas line included a dedicated pump-out port to facilitate changing of the gas species. That process involves an overnight bake of the source line from regulator exit valve up to input fitting of the leak valve. Two "oil filter" NEG pumps (figure 4) were added to the lower front, unoccupied 2-3/4" ports on the chamber (one visible in figure 3).

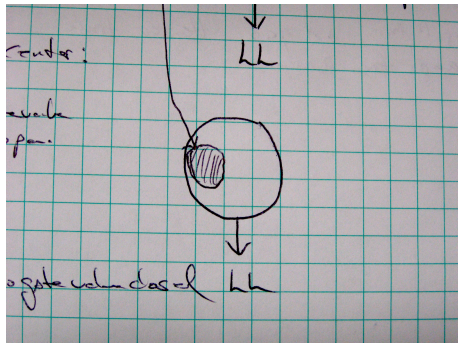

Figure 2. Photo of notebook page showing alignment of ion beam on phosphor plate.

Figure 3. New top flange (right) with RBD Instruments ion gun, rotary feedthrough attached to phosphor plate, current feedthroughs for alkali (Cs and Li) sources and viewport. Left, overall view of chamber showing leak valves (NF_3, noble gas for ion generation and CO_2), NEG pump (heater jacketed closed nipple) and 500 l/s ion pump.

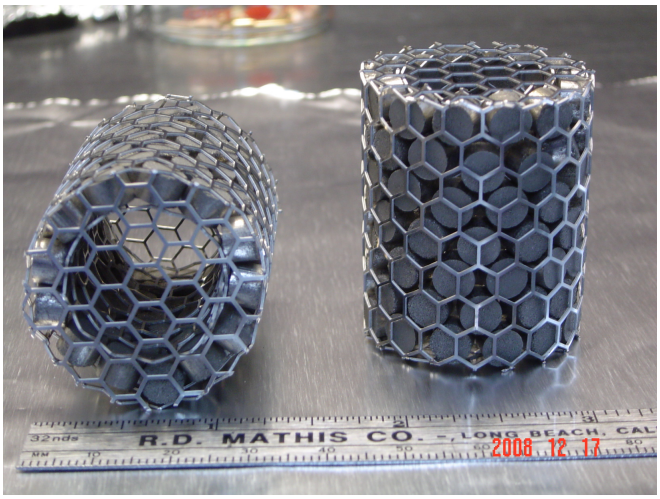

Figure 4. "Oil filter" ST707 NEG pumps fabricated in house. The stacking of the pellets allows maximum surface area exposure. The cages are etched SST spot-welded units. They achieve ~50% activation with bakeout alone.

At the pressures for which ion exposures will take place, it is necessary to be able to position the ion beam and measure its profile as the energy is changed since the flux is too low to easily be seen on the phosphor plate. To rapidly position the ion beam, a profiler/positioner was constructed (figure 5). It consists of a linear feedthrough which moves a dual purpose arm. Electrical contacts to the arm and inner electrode are brought out separately to dual BNC feedthroughs. The arm, when electrically tied together, can be used as a profiler by measuring absorbed current as a function of linear position. To cut down on the number of reflected particles, the end of the probe arm is beveled at 45°. Current versus position provides an integral of the beam shape; numeric differentiation yields the actual profile. When current is measured by the inner electrode, outer arm and sample (all with same value of (small) bias), the ion beam can be centered on the sample by: a) maximizing the current on the sample and inner electrode and b) minimizing the current on the outer probe arm. The probe arm and inner electrode can also serve as an ion beam block to even better define the area of access to the activated sample surface.

A closeup photograph of the profiler arm and the installed unit are shown in figure 6. The inner electrode is suspended in place by 4 alumina tubes. Three of the 4 are set-screwed in place. The fourth carries a connector wire (left side in photo) outside the profiler arm where it traverses parallel to the arm to the midpoint connection bar (not visible). Hand wound tantalum springs center-guided by rods parallel to the profiler arm provide the mechanical relief during travel for the electrode contacts as well as being the electrical leads connected to the BNC feedthroughs. The unit is attached to a 5-way mini-conflat fitting. Total travel of the unit is 2", with the knife edge extending beyond the far sample perimeter in the fully extended position. Profile data was acquired by manually operating the linear drive, with data from the profiler arm and the photocathode connected picoammeter meters collected in parallel by direct computer read-in with the required motion changes indicated by a computer generated audio signal.

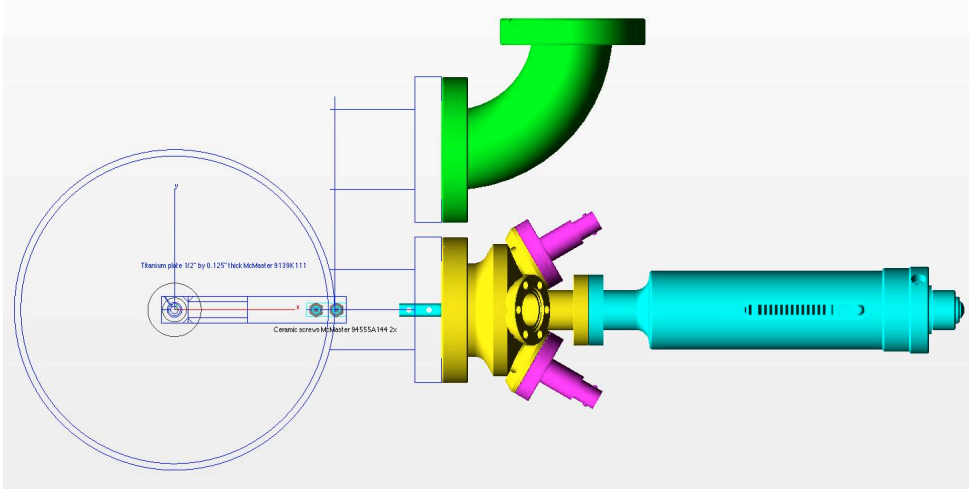

Figure 5. Beam profiler showing detail of profiling arm, linear feedthrough (blue), BNC connectors (magenta) and 5-way flange coupler (yellow).

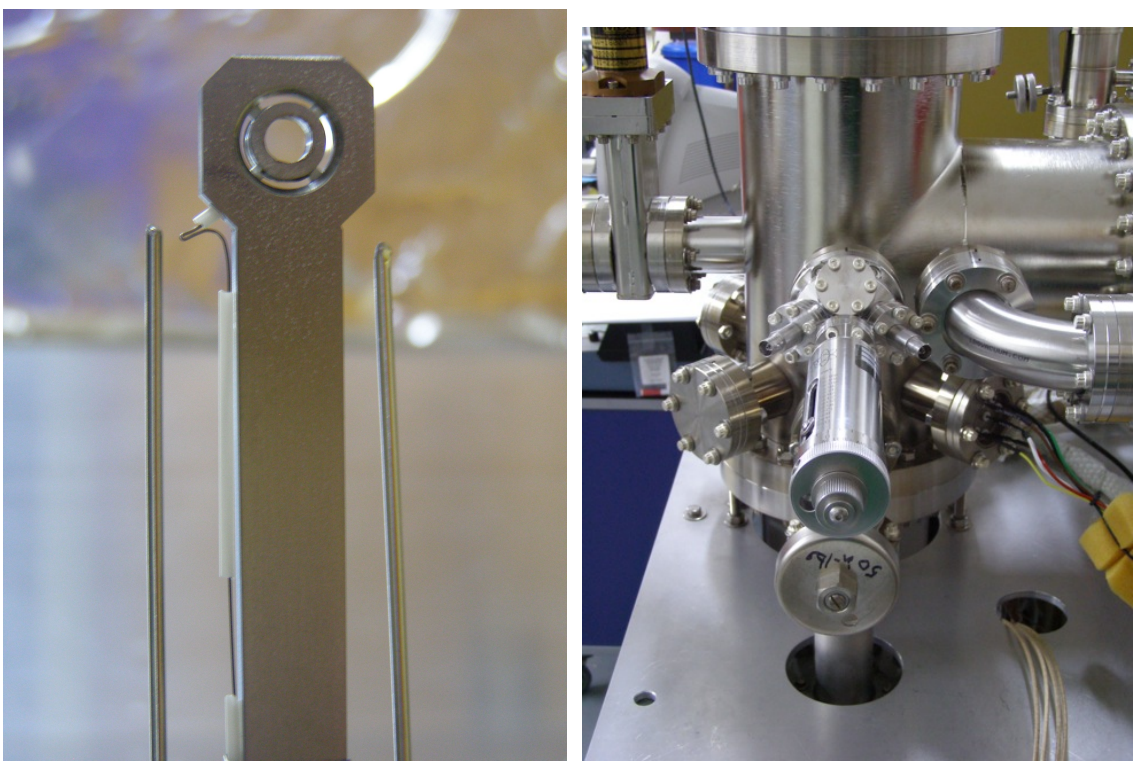

Figure 6. Beam profiler end (left) and unit installed on chamber (right). The rods are guides for the sliding spring contacts to the isolated center contact and the outer electrode. The two plates are attached to BNC feedthroughs. The large plate is beveled on the end allowing it to be used as a moving knife edge for profiling.

Quantum yield mapping take places by positionally scanning a laser beam through the viewport of figure 1. Custom software was written in LabView to control a two-axis Thorlabs

galvanometer mirror unit (figure 7). The same software was later employed for the scanner setup for the second photoemission test chamber. The control software includes provision to change the scanning range based on the viewport angle with respect to the sample so the distance between scan points remains constant for both of the two orthogonal galvanometers.

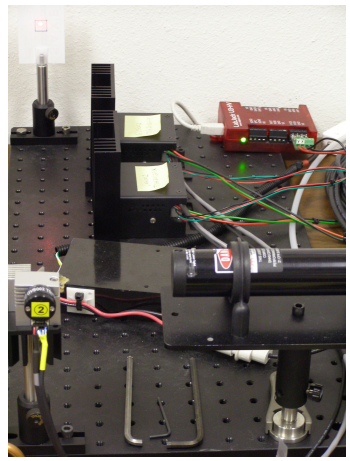

Figure 7. Galvanometer test setup. The two mirror scanner (lower left) is powered by programmable supplies (large heat sinks) controlled by a LabJack interface (red box, upper right). The scanners were set at the same distance to the target as they will be from the sample in the chamber.

Photoyield data taken as part of the recommissioning activities are plotted in figure 8. Data for both Cs and Cs+Li activated (NF_3 used for both) bulk GaAs are shown. The usual squaring–up of the photoyield curve near the bandgap, in comparison with the Cs activated material, is evident for the Cs+Li activated photocathode. Other recommissioning activities included setup of the photoyield scan system on the chamber (see below), improvements in the software control for easy ion beam profile data acquisition and commissioning of the ion gun.

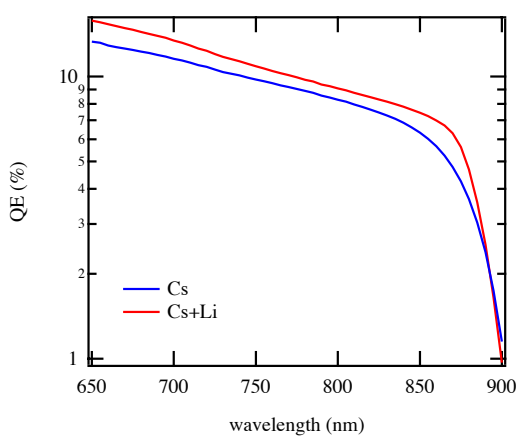

Figure 8. Cs and Cs+Li activated bulk GaAs photoyield as a function of wavelength taken as part of recommissioning chamber 1 (ion studies system).

Beam Profiles

Beam profile data were acquired using the combination of the profile/centering arm and sample. The arm in this mode had both the inner ring electrode and the outer arm biased together. The arm + ring and sample were biased to the same values by two distinct 300 V carbon–zinc batteries, each enclosed in a grounded shield box. Positive polarity with respect to the arm and sample was used to ensure capture of all secondary electrons so that the measured current would correctly represent the ion current. The bias did have the effect of reducing the effective ion energies, so the 1 kV setting on the ion gun supply corresponded to 700 V, while the 2 kV beam setting resulted in a net energy of 1.7 kV. Profile data were acquired with automated computer readout and recording of values from two Keithley 485 picoammeters via the LabView program shown in figure 9. The profile arm scans were performed by manually changing the arm position via a rotary–to–linear motion drive. Each profile took less than 5 minutes to acquire.

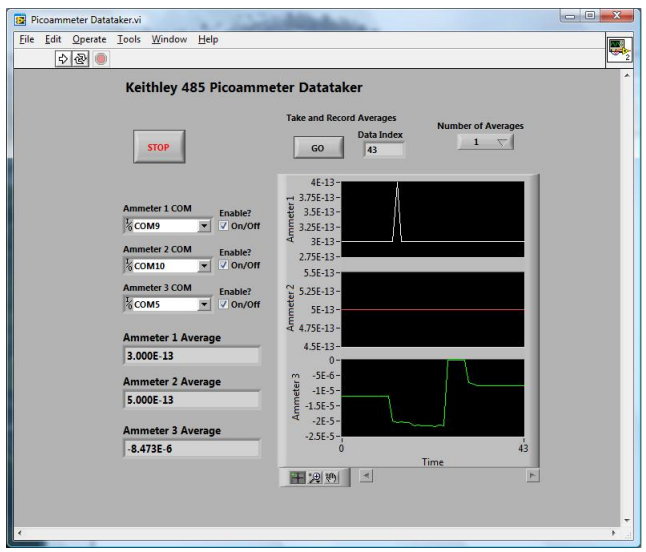

Figure 9. Screenshot of Labview program used to acquire beam profile data. Each of up to three picoammeters can be enabled for measuring the current on the profile arm, centering ring (tied together for these measurements) and the photocathode.

An example of the raw data for 2 kV Ar ion beam is shown in figure 10. By acquiring measurements using both the profile arm and the cathode, we obtained complementary data sets. Each set represents the integral of the current for the two collecting surfaces as the beam profile arm (cathode) exited (was exposed to) the ion beam. The data used in the subsequent analysis were taken with 4 times the spatial resolution of the data in figure 10.

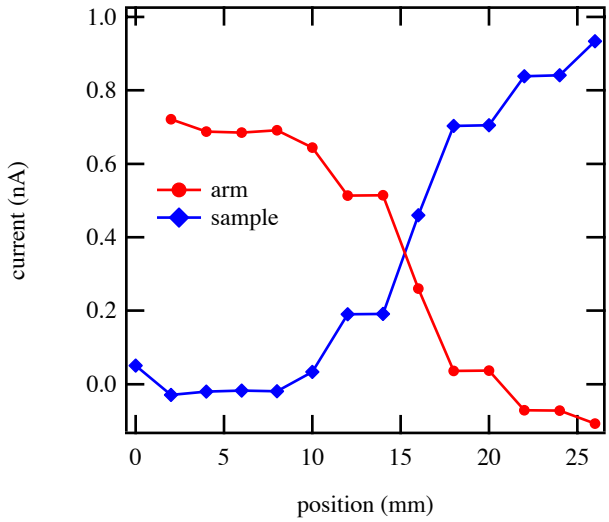

Figure 10. Integral ion currents from profile arm + centering ring and photocathode for 2 kV Ar ion beam taken with coarse resolution.

To reduce noise amplification from the numerical differentiation, the raw data were first smoothed, then differentiated. This resulted in the data sets shown in figure 11 and figure 12 for 1 and 2 kV Ar ion beams, respectively. The focus had been set up for the 2 kV beam, so it exhibited the better (narrower) beam profile.

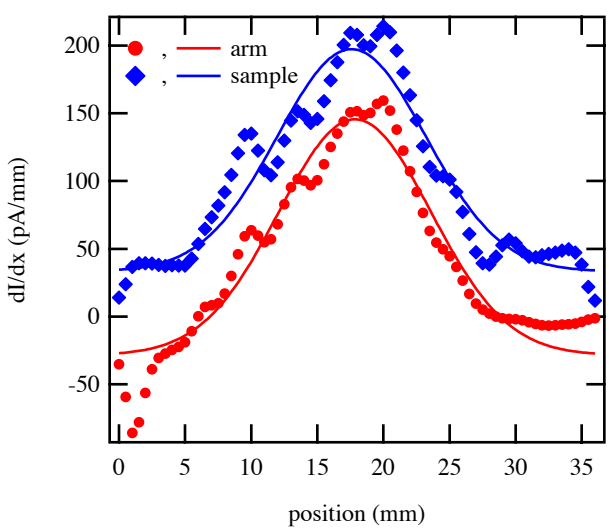

Figure 11. Profile data for 1 kV argon ion beam. The solid lines are Gaussian fits to the data.

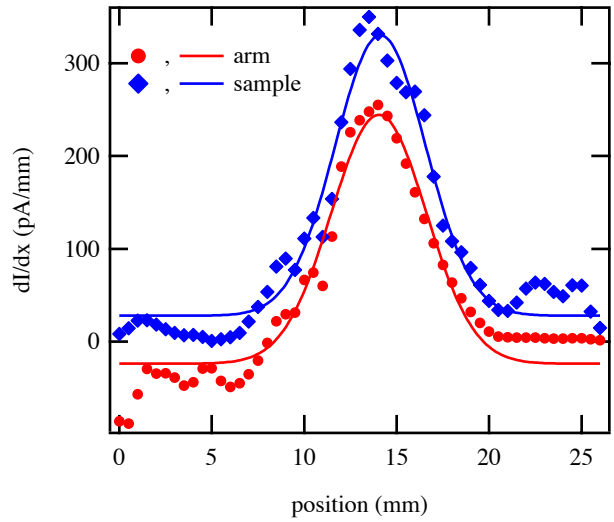

Figure 12. Profile date for 2 kV argon ion beam. The solid lines are Gaussian fits to the data.

The fits to the data are Gaussian, with the two complementary data sets yielding approximately the same values. The Gaussian parameters for each of the four fits are presented in table 1. These data and their analysis provided the necessary information for the generation of two–dimensional Gaussian curves representing the ion beam profile across the sample which in turn allowed the inference of the ion flux impinging on each scan point in the quantum efficiency maps resulting in the determination of the fractional quantum efficiency drop per ion for a given ion mass and energy as discussed in the section on Task 7.

Energy (kV)	Collector	σ (mm)	FWHM (mm)
1.0	Arm	5.8	13.5
1.0	Sample	5.6	13.2
2.0	Arm	2.6	6.0
2.0	Sample	2.4	5.7

Table 1. Gaussian fit parameters for the four data sets of figures 4 and 5.

Ion Flux

To calculate the effects on the quantum efficiency as a function of ion flux, it was necessary to acquire the actual ion current. This was done by first heat cleaning a bulk GaAs sample, but not activating it, so as to eliminate the effects of high secondary electron yield from the NEA surface. Ion currents were then generated and collected on the cleaned surface. A ceramic–stack switch enclosed in a grounded shield box allowed selection of bias direction and provided the option to either bypass the bias battery or to disconnect the sample completely from the picoammeter. For the available ion gun power supply energies, the sample current was measured for three conditions: no sample bias, negative sample bias and positive sample bias. The latter two changed the effective ion energy by +0.3 and –0.3 kV, respectively. These data are

summarized in table 2. The currents were measured with Ar contributing to raise the total pressure to $4x10^{-9}$ Torr from its starting value of $3x10^{-10}$ Torr.

Energy (kV)	I_{meter} (nA)	I_- (nA)	I_+ (nA)
0.5	3.40	4.01	1.36
1.0	4.90	5.80	1.94
1.5	6.61	7.50	2.46
2.0	8.20	9.93	3.00

Table 2. Currents measured on clean GaAs sample as function of Ar ion energy for no (I_{meter}), negative (I_-) and positive (I_+) sample bias. In the latter two cases, the sample bias was ±300 V. All currents measured positive.

From the data of table 2, it is apparent that the ion beam generates a sizable secondary electron current when interacting with the GaAs and Ta surfaces since the ion current alone is considerably less than the combined currents in either of the two other cases ($I_- > I_{meter} > I_+$). Some small difference may also be due to changing beam characteristics with the sample biased positive. Provided all other settings are repeated, these data can be used as estimators of the ion current in the absence of measured values for other Ar ion dosing experiments. However, it is preferable to measure the ion current at the onset of the ion dosing for each experiment with the sample temporarily biased positive even though this shifts the ion energy by 300 V for the brief interval during the measurement. The standard connection for ion dosing is with the control panel set to the "meter" position, i.e, no bias.

Task 2: Set up electron gun in training and interface test system

A non-loadlocked, stand alone photocathode test system, formerly used for amorphous SiGe photoemitter testing, was repurposed for training and interface setup demonstration for SLAC/SSRL personnel. The modifications included upgrading the cathode mount for higher temperature capability by changing the holder to solid molybdenum, moving the Cs channel source to the upper level and adding an electron gun and associated electrical feedthrough to the new, upper cross. The system had a bulk GaAs sample installed into it, was baked and then run through several activation/rejuvenation cycles to fine tune the parameters for optimal photocathode recovery. The reconfigured system in operation is shown in figure 13.

Dr. Kirby, as subcontractor to SLAC/SSRL, traveled to Saxet Surface Science in the week of November 14, 2010 to be trained on the operation of the system. This allowed him, together with SLAC/SSRL personnel, to be able to reproduce its setup at SLAC/SSRL. During Dr. Kirby's trip, the activation methodology for the training system, including heating time, cooldown period, channel currents and activation gas introduction pressure were presented. Electron beam rejuvenation was illustrated (figure 14) on a photocathode that had been allowed to decay several days after activation. The operational scheme was detailed as follows: With the laser on and stable (~1 hr), the photocathode is battery biased by -36V, positive end to the input of the electrometer. The laser intensity is controlled by a neutral density filter to keep the photocurrent

in the 100 nA range or below. The electrometer is set on a fixed scale, e.g., 30 μA (3 and 10^{-5} on the electrometer dials = 30 μA), to provide a measure of the DC component of the total current. Photocathode bias, chopper, and laser were on continuously during the photocurrent rejuvenation experiment, with the shutter closed when not measuring photocurrent. Data points were collected every minute or so by opening the shutter, letting the electrometer and lock-in settle for a few moments, then recording the data. The training system experiment ran with an electron gun current of 1-2 μA DC. The AC photocurrent (chopped) appears at the electrometer analog voltage output and is fed to the chopper-referenced lock-in. The output of the lock-in was acquired via its GPIB interface.

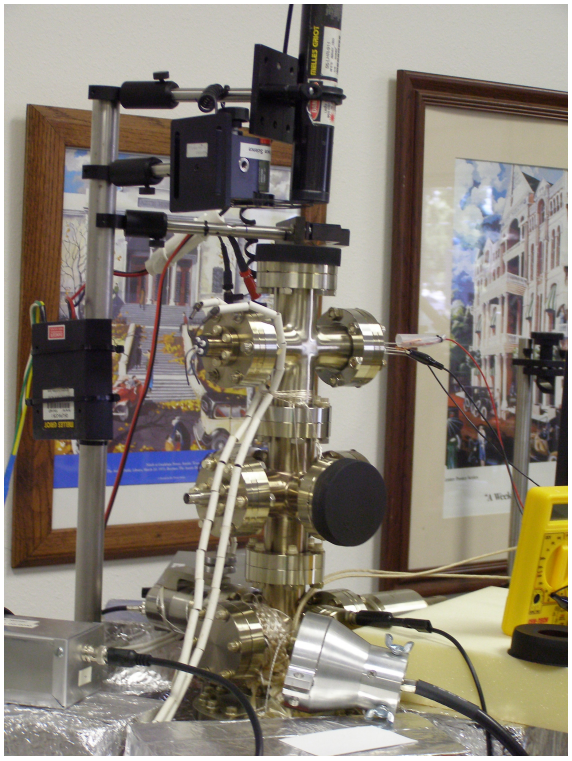

Figure 13. Electron rejuvenation training system. Electron gun, viewports, Cs channel and respective electrical feedthroughs are in upper cross. Sample, heater, viewport and sample contact feedthrough, middle cross. Leak valve, NEG pump, bake isolation valve and ion pump lower cross.

A followup teleconference which included Dr. Mulhollan and Mr. Bierman of Saxet Surface Science, Dr. Kirby, subcontracting to SLAC/SSRL, and Dr. Steven Sun of SLAC/SSRL took place November 29, 2010. In this meeting, it was decided that the following equipment, in lieu of the entire test chamber, would be shipped to SLAC/SSRL:

1. A Kimball-Physics electron gun, with controller, grid bias power supply and connection wires. Saxet will mount the gun on a 4-pin CF feedthrough flange allowing a 3 inch gap to the chamber center. Also included will be a small multimeter for in-line monitoring of the grid bias current.
2. An SRS electronic chopper and electronic shutter with TTL 5V control box fabricated in house at Saxet.

3. An SRS 510 lock-in-amplifier and desktop Keithley 610C electrometer, with a 2-pin to BNC output cable.
4. Cs and Li channel alkali sources.

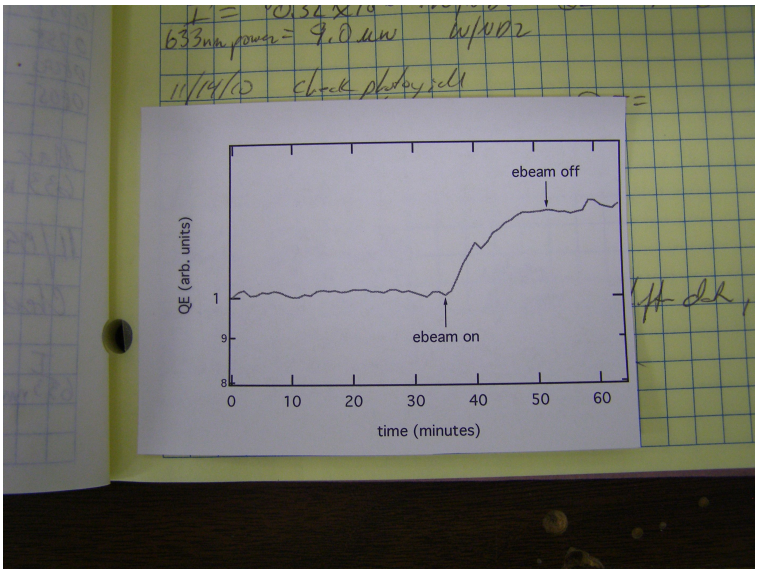

Figure 14. Photo of lab notebook showing data taken on 11/15/2010 during training visit of Robert Kirby to Saxet Surface Science.

NOTE: TASK 3 AND TASK 5 WERE CONSOLIDATED
Task 3: Interface acquisition subsystems into SSRL acquisition system
Task 5: Set up and conduct at SSRL electron beam recovery measurements
These two tasks are combined in the report since they were displaced to an earlier time than originally scheduled, though still within the first year.

The intent of this work was to determine what, if any, discernible changes in the surface composition and/or activation layer structure following electron beam rejuvenation of the partially–decayed NEA surface could be detected via XPS and valence band photoemission. The samples were prepared for activation as described in ref. [1]. The activations followed the standard Cs+NF_3 and Cs+O_2 procedures. Activations were followed by CO_2 and electron beam dosing. Photoemission spectra were collected by a PHI hemispherical electron energy analyzer at beam lines 8–1, hν = 30–170 eV, and 10–1, hν = 200–1000 eV, of the Stanford Synchrotron Radiation Lightsource (SSRL) and were normalized by photon beam flux. Cathode quantum efficiency during CO_2 and electron beam dosing was monitored as described in ref. [2]. The CO_2 partial pressures and secondary electron currents employed are noted in the corresponding figures.

A Kimball Physics electron gun, model FRA-2X1-2Th, was provided to the SSRL group for use as the electron source. This gun was the same model as the one used in the demonstration system at Saxet (later moved to the test chamber). The gun was acquired as an unmounted unit, so a simple mounting and alignment feedthrough assembly was fabricated. Front and side views of

the mounted gun are shown in figures 15 and 16, respectively. The sample to gun distance for the SSRL end station was set to mimic that of the demonstration system at Saxet. Electrical connection was through a four-pin feedthrough flange (only three pins used). Due to the construction of the Kimball Physics EGPS-7H power supply, the grid voltage had to be provided from a separate unit. The operating points for the twin of the gun supplied to SSRL were 1000 V on the Kimball-Physics supply, 973 V on the Trek (grid) supply and a filament current of ~ 1.65 A as metered by the Kimball Physics supply. Saxet also provided alkali channel sources for the experiment.

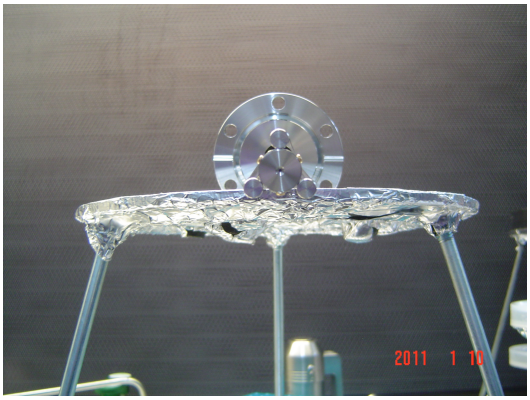

Figure 15. End view of mounted Kimball Physics electron gun. The three rods act to center the gun, clamp it in place and provide the ground connection to the outer cylindrical electrode.

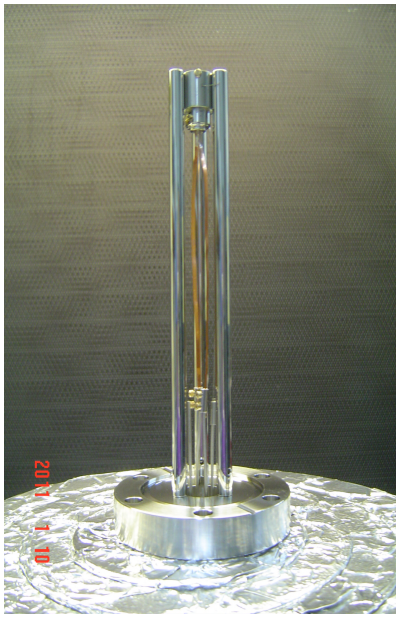

Figure 16. Side view of mounted Kimball Physics electron gun. The ribbons are the filament connections; the wire supplies the grid voltage.

Quantum efficiency following CO_2 (left) and electron beam (right) dosing are shown in figures

17 and 18. The quantum efficiency was made to drop at a rapid, but well controlled rate upon leaking in CO_2 at $3x10^{-9}$ Torr. For both the $Cs+NF_3$ and $Cs+O_2$ activated surfaces, the decay rate was equivalent, i.e., susceptibility to CO_2 for either activation recipe was about the same. As reported in the Phase I work and ref. [2], the behavior upon electron beam dosing was vastly different for the $Cs+NF_3$ and $Cs+O_2$ activated surfaces.

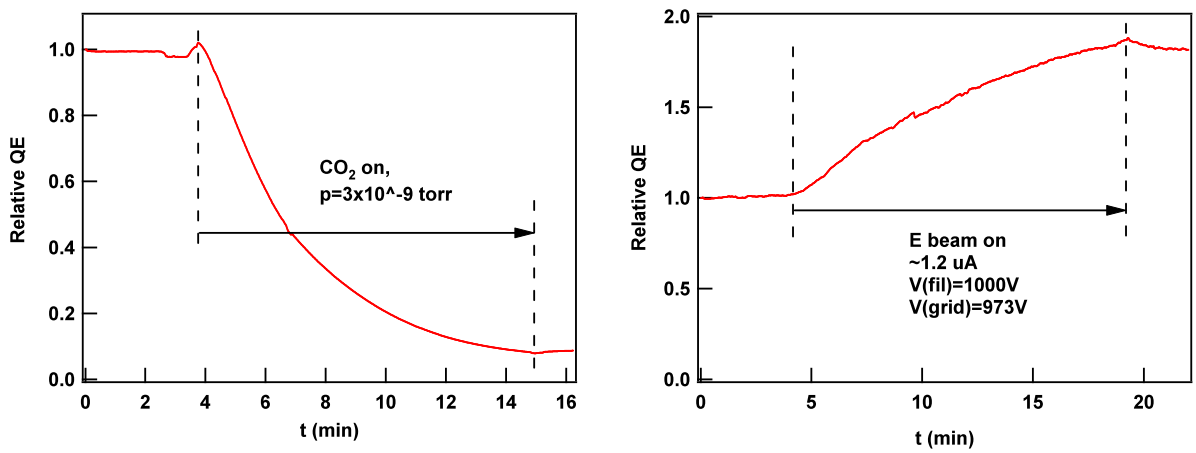

Figure 17. $Cs+NF_3$ activated GaAs change in QE with CO_2 dosing (left) and electron beam application (right).

In the case of the $Cs+NF_3$ activated GaAs, the electron beam, post CO_2 exposure, caused the quantum yield to recover, while for the $Cs+O_2$ activated GaAs, the electron beam induced an even greater drop in the quantum efficiency. This is the exact behavior as seen in the Phase I work at Saxet, though the sizes of the effects were somewhat different. The difference is likely due to a combination of cathode material, electron flux (beam size) and chamber chemistry. In both cases, the electron beam gun settings and total (secondary + reflected primary) electron beam currents were the same as used in the Saxet demonstration system tests discussed earlier.

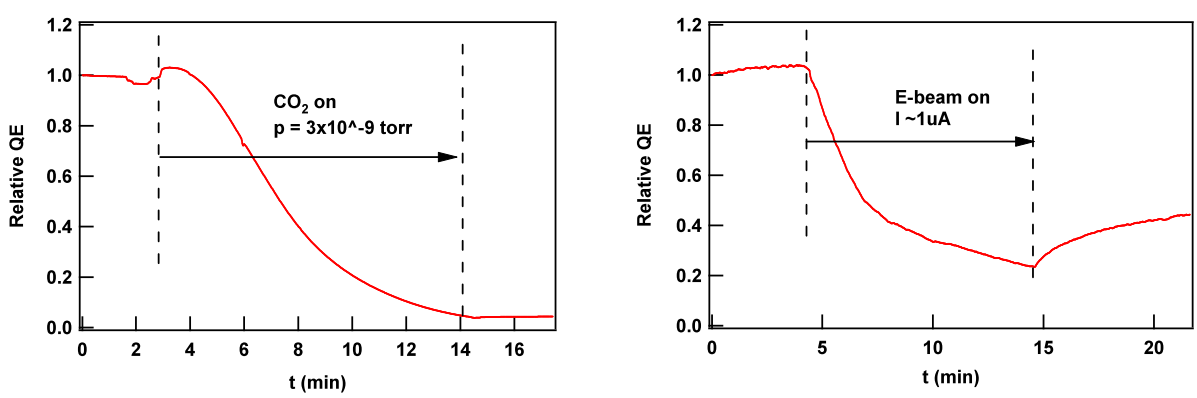

Figure 18. $Cs+O_2$ activated GaAs change in QE with CO_2 dosing (left) and electron beam application (right).

XPS and valence band photoemission data were acquired first on SSRL beam line 8-1. Data were taken following the CO_2 exposure and after the electron beam dosing. The data for the Cs+NF_3 activated surface are shown in figures 19a and 19b. The data for the Cs+O_2 activated surface are shown in figures 20a and 20b. The accessible core levels on the 8-1 beam line were As 3d, Ga 3d and Cs 4d. No change in the shape or intensity of either the core levels or valence band was detected for the Cs+NF_3 activated photocathode following application of the electron beam.

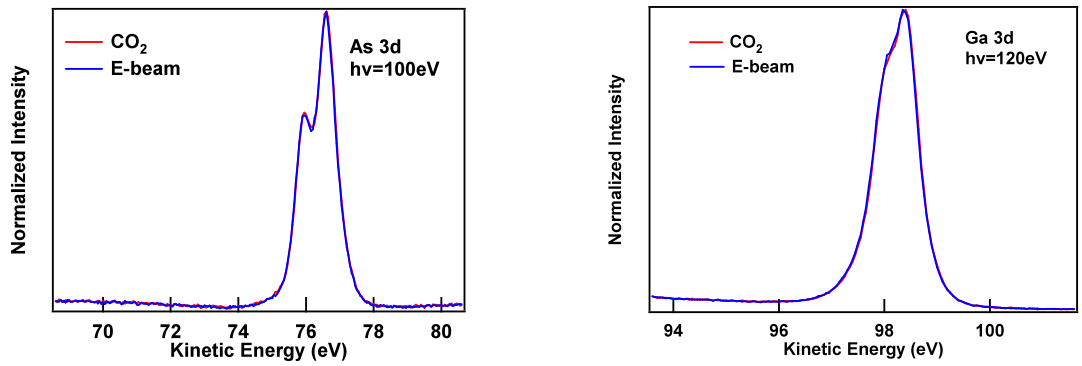

Figure 19a. As 3d and Ga 3d core level spectra for the Cs+NF_3 activated photocathode following the treatments shown in figure 17. The data show no change in the core levels' positions or sizes after the electron beam application.

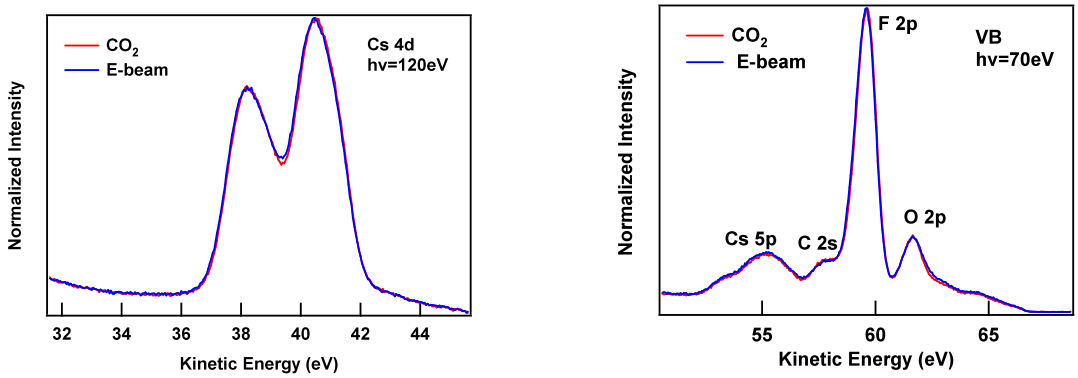

Figure 19b. Valence band and Cs 4d core level spectra for the Cs+NF_3 activated photocathode following the treatments shown in figure 17. The data show no change in the core level or valence band peaks' positions or sizes after the electron beam application.

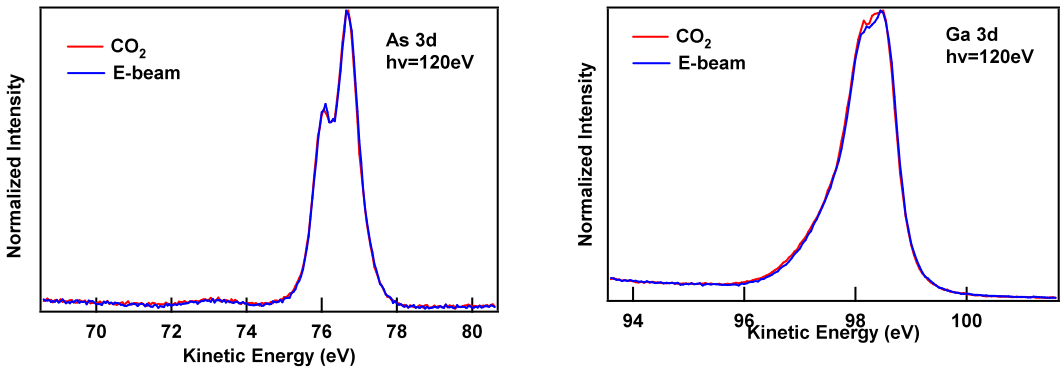

Figure 20a. As 3d and Ga 3d core level spectra for the Cs+O_2 activated photocathode following the treatments shown in figure 18. The data show no change in the core levels' positions or sizes after the electron beam application.

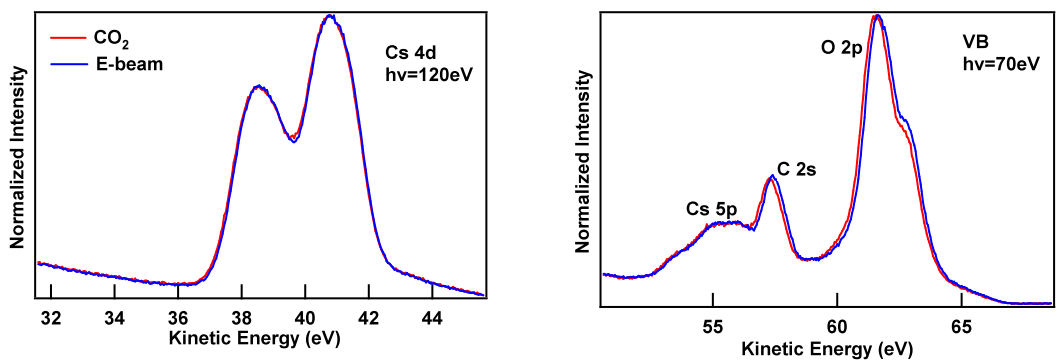

Figure 20b. Valence band and Cs 4d core level spectra for the Cs+O_2 activated photocathode following the treatments shown in figure 18. The data show no change in the core level or valence band peaks' positions or sizes after the electron beam application.

The second block of data were acquired on SSRL beam line 10-1 which has higher photon energies available. The data for the Cs+NF_3 activated photocathode are shown in figure 21. It was necessary to normalize the data by the (not shown) Ga 3d intensity to properly scale the results. Small drops in the O 1s and C 1s core levels along with a small decrease in the F 1s are apparent. The former would suggest that the electron beam acts to partly desorb previously absorbed CO_2 from the activated surface. The latter effect was further explored by application of the electron beam to an activated, but non-CO_2 dosed surface. Those data appear in figure 22a and 22b.

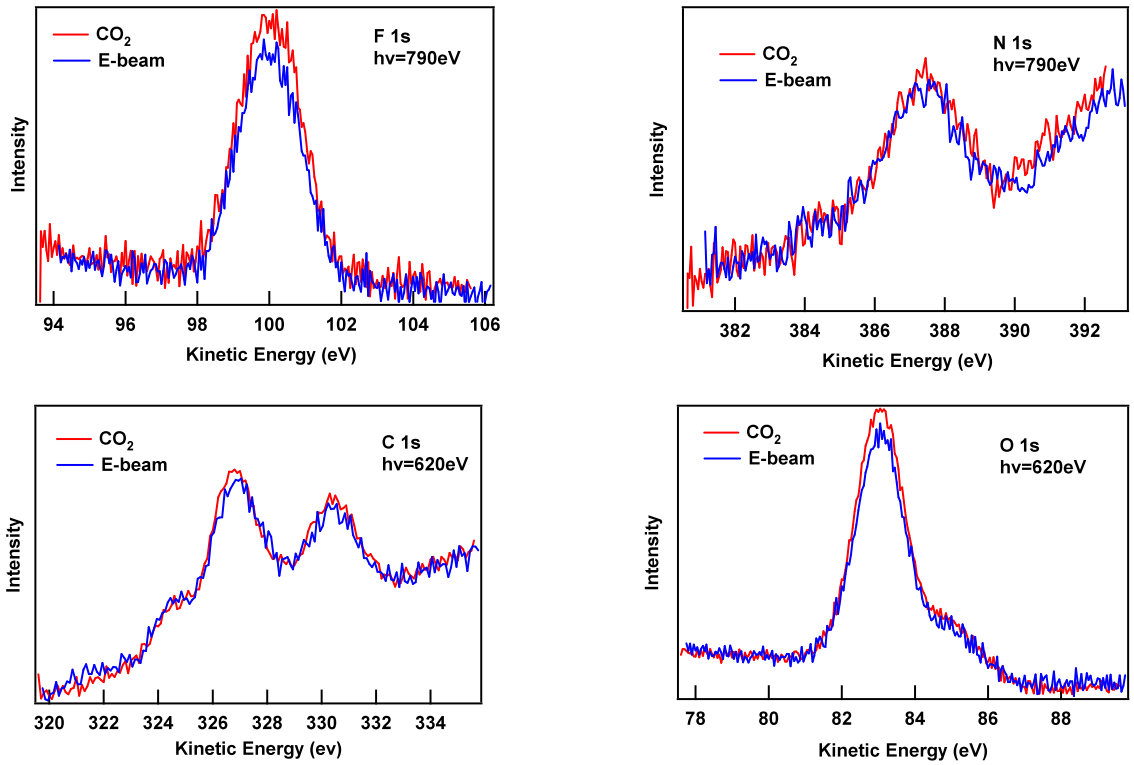

Figure 21. Cs+NF_3, normalized to the Ga 3d intensity. Clearly visible is a reduction in the carbon and oxygen peaks, accompanied by a slight reduction in fluorine as well.

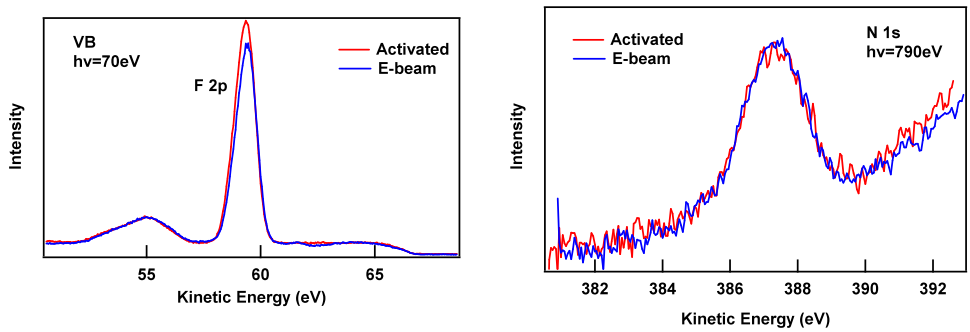

Figure 22a. Valence band and N 1s core level spectra of electron dosed surface.

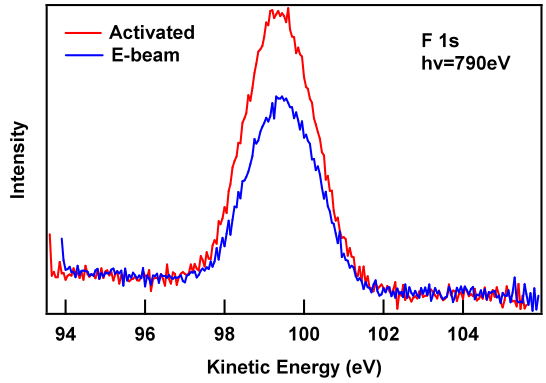

Figure 22b. F 1s core level spectra of electron dosed surface without CO_2 dosing.

Interestingly, while the F 1s core level and F 2p valence band signals decreased, the N 1s signal was stable. The quantum efficiency during the operation did not change, i.e, the partial rearrangement or desorption of the fluorine did not impact the electron affinity! The effects on the Cs+O_2 activated surface were much stronger as seen in figure 23.

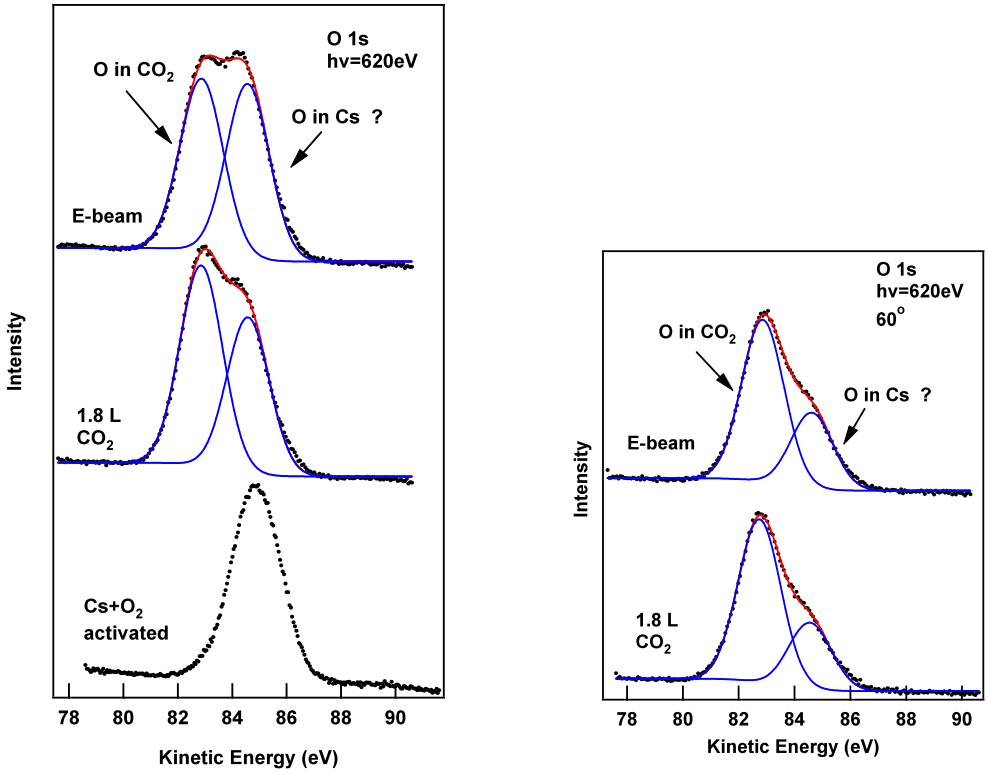

Figure 23. O 1s core level for normal (left) and large angle (right, 60°) emission angles for activated plus CO_2 and electron beam dosed surfaces. The change in peak size with angle indicates that the electrons comprising the higher kinetic energy peak originated from below the location where the lower kinetic energy peak electrons originated, i.e., the CO_2 was adsorbed atop the activation layer.

By varying the emission angle, relative depth information can be obtained. Prior to CO_2 adsorption, one O 1s peak existed. Following CO_2 adsorption a second chemical state of the O 1s core level emerged. Electron beam dosing of the CO_2 decorated surface resulted in an equalization of the two O 1s peak intensities. The surface sensitive spectra at 60° show that the O 1s due to the presence of the CO_2 was adsorbed on top of the activation layer, which was the origin of the original O 1s peak. The action of the electron beam on the Cs+O activated surface seems to have been to crack the CO_2 molecules and allow the migration of more O into the Cs+O underlying activation layer. Chemical absorption studies at Saxet have shown that oxygen in the form of O_2 has a much stronger effect than CO_2 in dropping the quantum efficiency. It is likely that an excess of O diminishes the QE more than chemisorbed, but intact CO_2 molecules. Additional information comes from examining the C 1s core level spectra shown in figure 24.

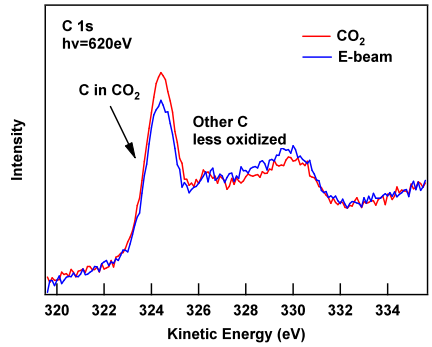

Figure 24. Carbon 1s core level spectra for CO_2 and electron beam dosed surfaces.

In the Cs+NF_3 activated surface (figure 21) there are 3 distinct C 1s peaks at ~325, 327 and 330 eV kinetic energy. In the data of figure 24, there is one strong peak at ~325, a second at 330 and several shifted together over the range from 326 to 330 eV. Not only are the relative distributions of the C 1 s peak in binding energy different, but the Cs+O_2 activated surface provides many more configurations for the C–to activation layer surface bonding. Based on the C 1s and O 1s absolute intensities, the sticking coefficient of CO_2 on the Cs+O_2 activated surface is 2-3 times larger than for the Cs+NF_3 activated one.

A complete explanation of why the quantum efficiency recovers for the Cs+NF_3 activated photocathode upon the application of an electron beam was still not forthcoming following the photoemission experiments. However, some insight was gained as to why Cs+O_2 activated photocathodes do not exhibit the same quantum efficiency recovery following application of an electron beam.

Task 4: Design chamber modifications for electron stimulated recovery studies

A new top flange for the second Saxet photocathode test chamber to accommodate the two types of guns: the Physical Electronics 04-015 electron gun (5 kV maximum) and the Kimball Physics FRA-2X1-2 low energy electron gun (50 eV - 1.0 keV) was designed. The flange provides an off-angle (~8°) viewport for sample access. A CAD drawing of the outlines of the top flange mounted atop the chamber is shown in figure 25. A beam profiler as detailed above was assembled and installed into the system through a 4-1/2” tee, all other details the same as the previous design. Cs and Li alkali channels were mounted from the side of the chamber on feedthroughs installed in the integral mini-conflat ports. A second leak valve was included to provide the decay accelerant (CO_2) for lifetime testing. The electron beam profiler (duplicate of the ion profiler), prior to installation, is shown in figure 26. The profiler installed into the chamber, immediately prior to baking is shown in figure 27.

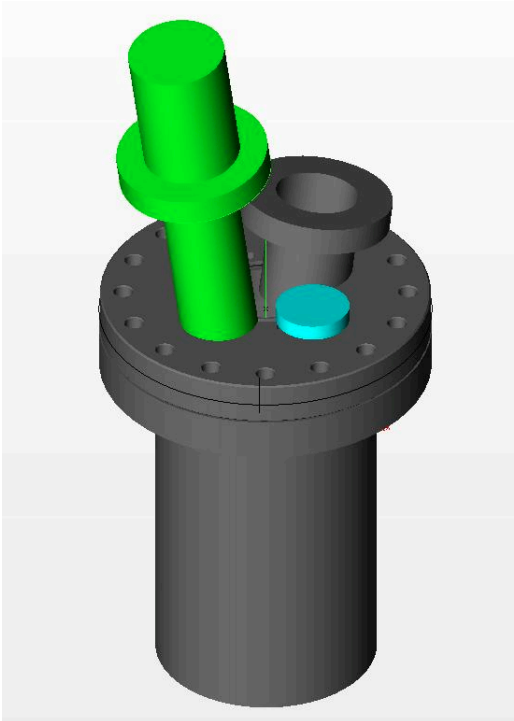

Figure 25. CAD drawing of top flange fabricated to house Physical Electronics electron gun, viewport and electron feedthrough for Kimball Physics electron gun (to be mounted internally).

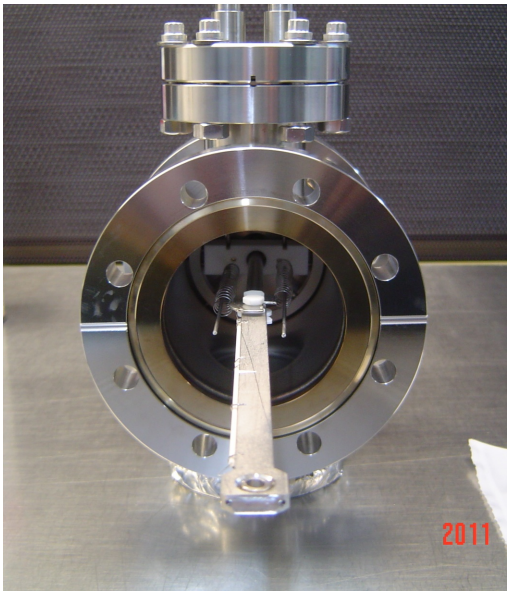

Figure 26. Profiler assembled and ready for installation on chamber 2.

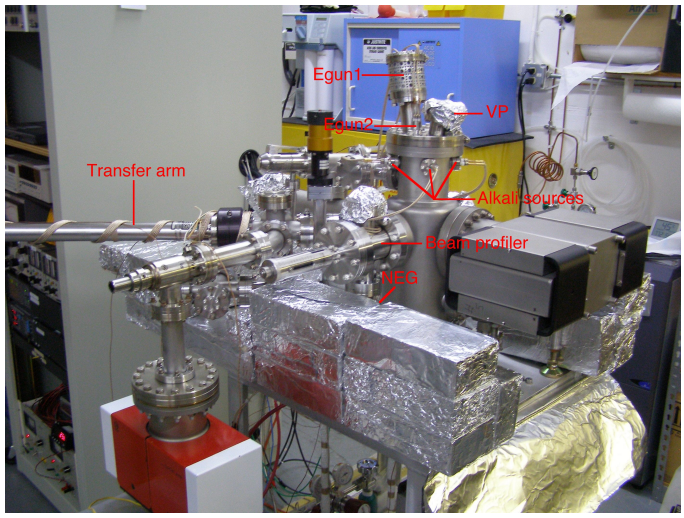

Figure 27. Chamber 2 (for electron beam rejuvenation studies) immediately prior to baking. Locations of the newly installed items are noted as is the loadlock transfer arm. The parallelepipeds are foil wrapped fire bricks used to extend the bakeout oven height.

Task 5: See Task 3

Task 6: Yield map setup

The mapping setup (before installation) was described in part above. Briefly, the scan system consists of a two axis galvanometer assembly under computer control via a custom written LabView program. Data are acquired along two orthogonal axes and stored as an array in tab–delimited text format. This makes the data both easy to display (in e.g., image or contour format) and to manipulate with most analysis programs. Scan speed is limited by the photocurrent settle time. A 21x21 array takes just over 7 minutes to acquire. An example set of data presented in image and contour format appears in figure 28.

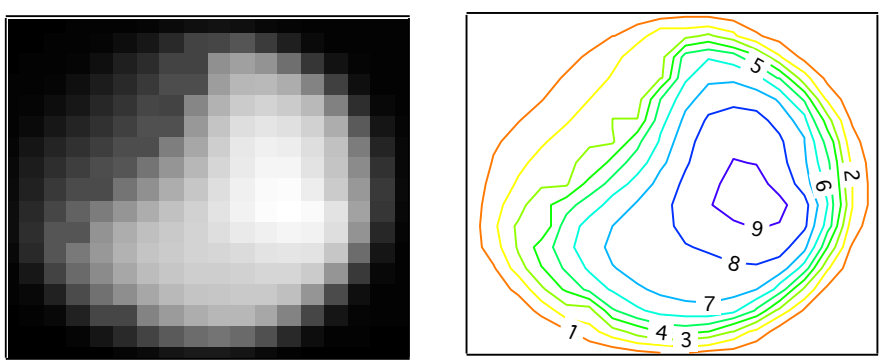

Figure 28. Example 21x21 photoyield scan of sample following Ne ion dosing at 2 kV presented as greyscale image (left, white = high photoyield) and rainbow contour (right, numbers indicate photoyield) plots.

To characterize photoemitters representative of both highest currents (bulk GaAs, short wavelength excitation) and high polarization/shortest pulses/low energy spread (thin GaAs, near bandgap excitation) both sample composition and photoyield monitor wavelengths were changed. So as to simplify the daily operation of the yield mapping feature on both the ion and ESR test systems, beam combiners were added to allow the visible (HeNe) light source to be used for alignment for both the visible and IR laser scanning conditions. Rather than physically swap the galvanometer head and control electronics from system to system, a second set was acquired. However, the second set was a very low cost 'consumer-grade' system, which was dichroic coated for the visible range. To allow efficient IR reflection by the two galvanometer mirrors, they were in-house recoated with aluminum. This greatly enhanced the total IR overall transmission while maintaining the HeNe throughput at nearly its original high value. The scan software was upgraded to allow input of the scan laser wavelength

Task 7: Ion species and flux measurements

Activated GaAs photocathodes had their near surface regions, including the activation layer, disrupted by application of an ion beam, thereby lowering the quantum efficiency. Post ion–exposure, susceptibility to a contaminant gas – in this case CO_2 – was determined. In the first step, the photocathode was exposed to a noble gas ion beam positioned near its periphery for 10 minutes. The subsequent CO_2 exposure times were as noted. An example of before and after ion dosing appears in figure 29. Also shown is the difference between the two datasets, clearly illustrating the position and shape of the ion beam. The example analysis is to be taken as 'in progress' and extracted values, etc. are subject to change in future.

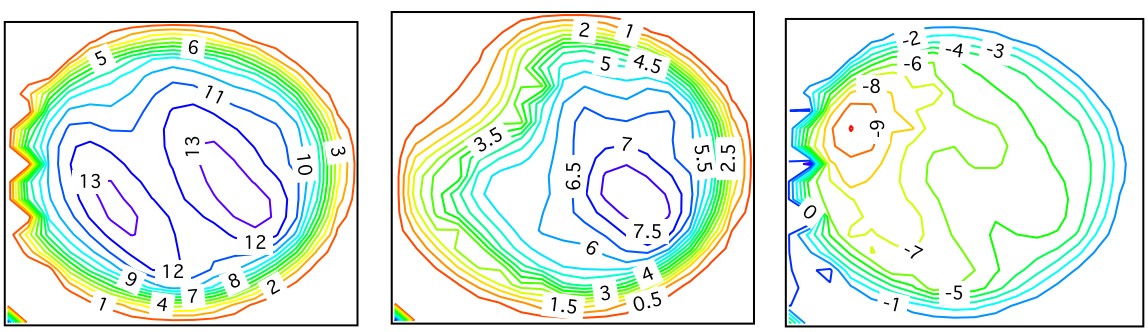

Figure 29. Contour plots of the photoyield following peaking up (left), after ion dosing (middle) and the difference in the two data sets (right). The ions were 2 kV Ne. The center of the ion beam is apparent in the photoyield difference plot at the most negative contour, -9%.

<u>Ion effects analysis</u>

The goal is to quantify the photoyield drop per ion at specific energy followed by quantification of the photoyield drop induced by CO_2 exposure at like ion flux locations. This allows us to determine if the ion damage caused an increased chemical sensitivity, i.e, faster decay rate upon CO_2 exposure. Initially, the cathode quantum efficiency was monitored by a HeNe laser (632.8 nm) scanned across the surface by a rotating mirror galvanometer system. The scan area was

generally divided into an odd numbered square array which included regions of the Ta photocathode clamping disk. Array scan times were ~4 minutes for 11x11 arrays and ~7 minutes for 21x21 arrays. Photoyield measurements were obtained prior to peaking up the photocathode (activated the previous day), immediately following peak up, after exposure to the ion beam, and at intervals corresponding to exposure to CO_2 using the indicated pressures. The photoyield measurements immediately following peaking up were used as a baseline for quantifying the changes due to ion or CO_2 exposure. An example set of photoyield scans normalized to fractional change is shown in figure 30.

Laser beam profile data was collected to quantify the width of the HeNe laser relative to the sampled area in the galvanometer scans. The HeNe beam had a Gaussian profile that spread its energy out uniformly in azimuth, while decreasing as a function of radius. A profile is shown in Figure 31. The profile was measured at distance of approximately 15.25″ from the final mirror in order to duplicate the distance induced spread from transmission to the sample within the vacuum chamber. The $1/e^2$ width was determined to be 1.3 mm, while for an 11x11 scan, the distance between scan points was 1.2 mm. Overlap is minimal for such an array. Halving the step size increases the overlap, but better samples the regions between the points of an 11x11 scan.

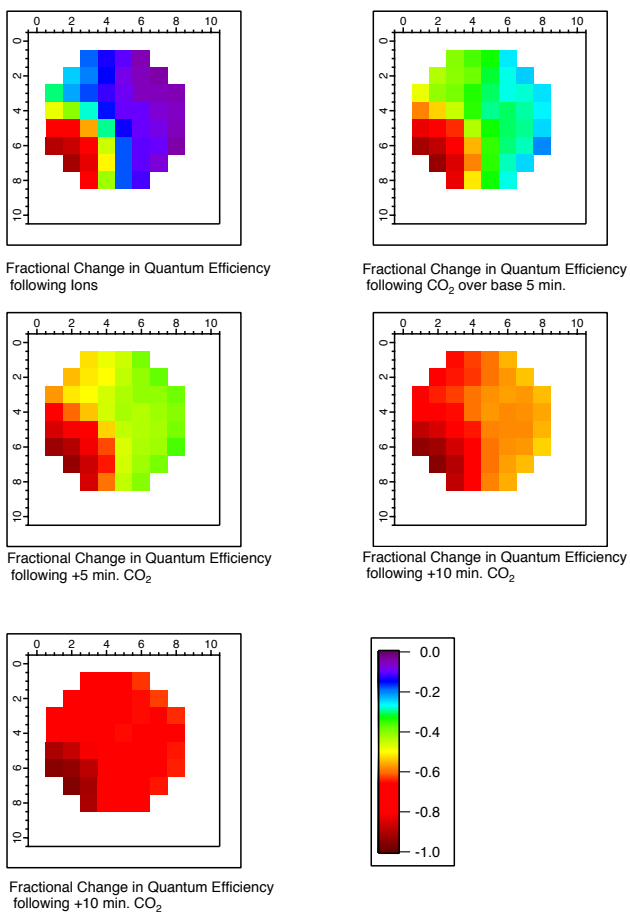

Figure 30. Two-dimensional false color plots of fractional change in quantum efficiency. The ions were 2 kV Ar. The laser scan size was 11x11.

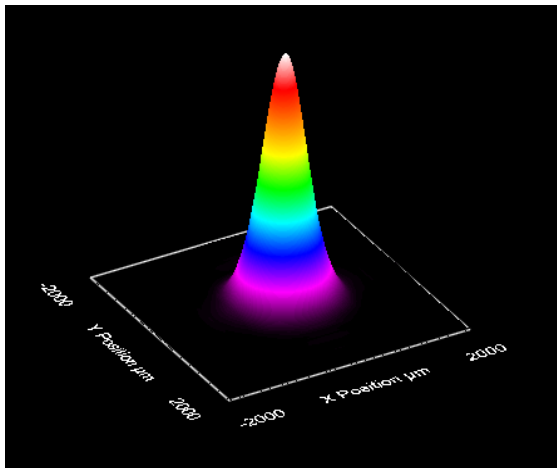

Figure 31. 3d plot of the HeNe laser beam profile. The inscribed square covers 4 mm along each axis.

The ion dosing data were analyzed as follows. First, a threshold was selected to cut off measurements outside the area of the cathode. The threshold value was ~10% relative to the maximum photoyield in the first, baseline photocathode dataset (following peaking up). All subsequent datasets were then adjusted to only include data from the same grid positions as the threshold–limited dataset. Next, the fractional change in photoyield relative to the baseline was computed and plots were generated to illustrate the progressive drop in performance following ion dosing and exposure to a dosing gas. Color mapping was performed such that identical colors represent identical data values across the representative plots.

Numerical values were extracted by starting with the shape parameters of the ion beam as obtained using the Gaussian fits of data obtained from the ion beam profiler as discussed on page 11. Alternative methods of modeling the ion beam, such as extracting its shape directly from the fractional change plots have also been used, but primarily to confirm the extracted beam profiles pass a 'reasonable value' test. Gaussian beam profiles were generated that were centered near the peak of the change in quantum efficiency data. The fraction of the 2d Gaussian that covered the scan region was then used to calculate the ion current in that area and then, based on exposure time, the total ion dose was extracted. These data were then used to extract the fractional change in the quantum efficiency per ion. Collected values for bulk GaAs at 633 nm appear in table 3.

Ion	Mass (AMU)	Ion Energy (kV)	Current (nA)	Total Ions	Photoyield drop per ion
Neon	20	2	0.59	2.22×10^{12}	2.7×10^{-10}
Neon	20	1	0.18	6.75×10^{11}	1.4×10^{-9}
Argon	40	2	3.0	1.1×10^{13}	6.0×10^{-12}
Argon	40	0.5	1.36	5.1×10^{12}	9.0×10^{-11}

Table 3. Extracted ion induced drop in photoyield for the indicated noble gas and energy.

CO_2 dosing analysis

This analysis is used to determine the effects the ion dosing has on the sensitivity of the activated surface to subsequent background gas reaction. The sample data shown in figure 32 are for a 1 kV Ne dosed surface. The region where the ion caused a decrease in the photoyield is very apparent. At first glance, it would appear that the ion dosed region is more robust with respect to CO_2 dosing than the undamaged region. However, inspection of figure 33, a single scan point variation of photoyield with time, shows the exponential form of the decay. If the decay were to begin at a lower point, such as with the ion dosing region, then the fractional change would be smaller with time. The proper way to illustrate this (or disprove the argument) is to plot the decay curves for the regions and shift the decay curve for the damaged area to the same value for the lesser affected area and see if the curves match up. For the shown data set, this is not possible since the exposure times were longer for the latter two plots. Later sets were collected with uniform intervals to allow this important comparison.

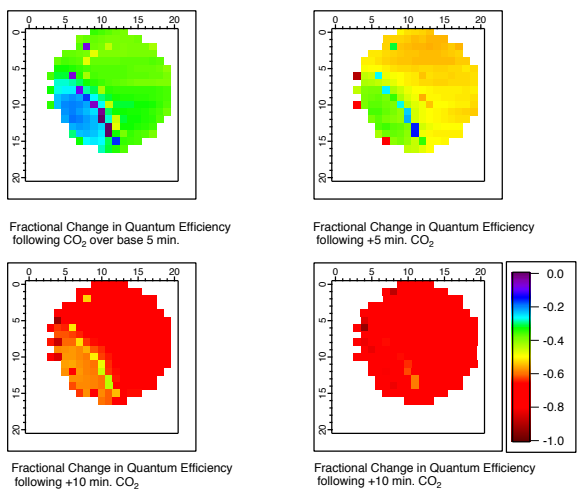

Figure 32. False color representation of the fractional change in photoyield due to CO_2 exposure following the Ne ion dosing at 1 kV. The scan size was 21x21.

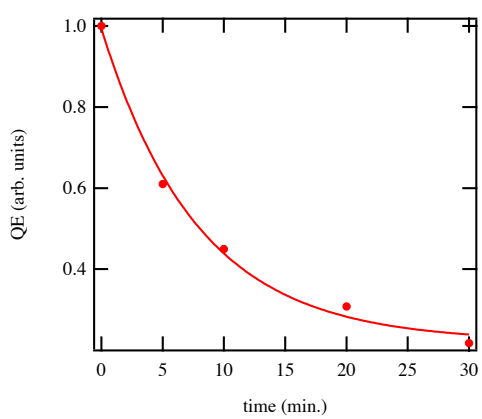

Figure 33. CO_2 induced photoyield drop as a function of time for a single scan point of an Ar ion dosed photocathode.

The same technique has been used to extract the parameters for the measurements of the ion effects on thin GaAs using a near bangap (846 nm) IR monitor laser. Rather than tabulate the partial results in this report, the complete analysis will be published in the open literature. The final results will appear as tables of mass and energy effects on photoyield for H (added to the gas list), He, Ne, Ar, Kr and Xe ions with energies ranging from 0.5 to 2.0 kV and for activations using Cs and Cs + Li. An example data set of the photoyield drop caused by 2 kV He ion and CO_2 interactions is shown in figure 34.

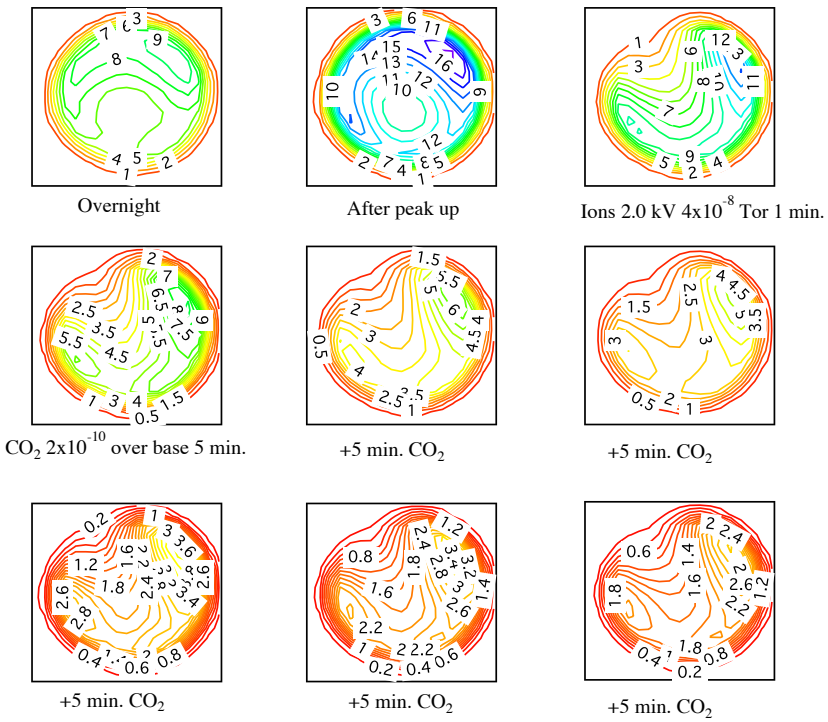

Figure 34. Contour plots showing the photoyield progression for a photocathode just prior to– and immediately following–peaking up with Cs through 2 kV He ion dosing, and the subsequent sequential CO_2 exposures at $2x10^{-10}$ Torr over the base pressure. The sample was Cs+NF_3 activated bulk GaAs with the photoyield measured at 633 nm.

Ion dosing effects on the photoyield have been measured on both Cs and Cs+Li activated surfaces. Comparison data using the same exposure sequence as shown in figure 34 are presented in figure 35 for 2 kV hydrogen. The final maximum relative photoyield (final frame, bottom right, each set) is significantly greater for the Cs+Li activated surface. The Cs+Li surface showed a factor of 3 drop overall, while the Cs only activated surface showed a factor of 6 drop. This is the expected behavior for NEA surfaces made with the improved activation method. The photoyields near the centroid of the ion beam (normalized to the starting photoyield) for the two styles of activated surfaces do show ~20% less drop for the Cs+Li activated surface in this case.

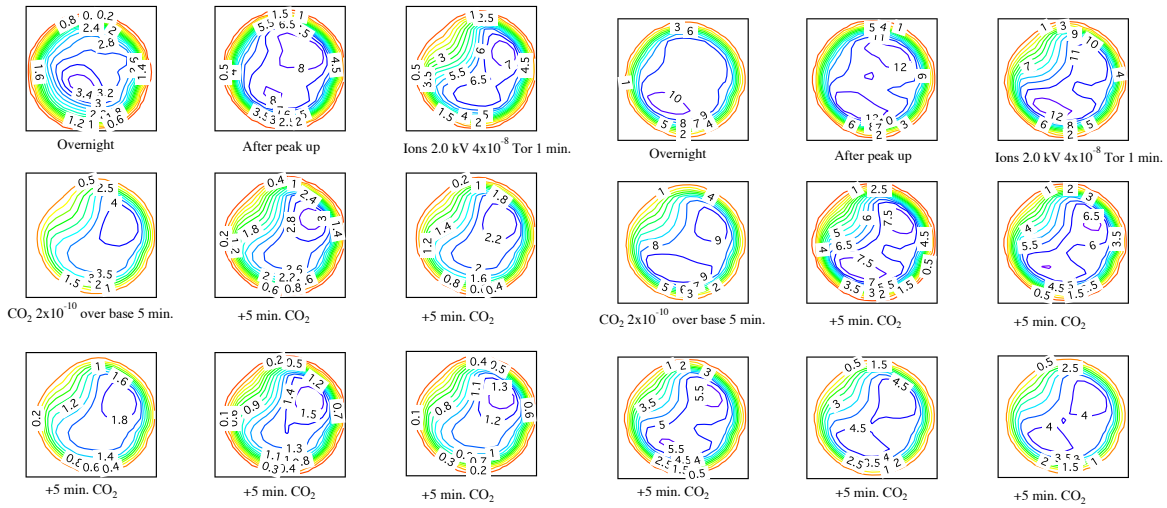

Figure 35. Contour plots showing the photoyield progression for a photocathode as in figure 34 for Cs only (right) and Cs+Li (left) activated surfaces.

An interesting and useful result was obtained when a heat cleaned GaAs surface was pre-bombarded with 2 kV Xe ions before activation. This experiment was to better determine the spacial localization of the ion damage, i.e., how much of the drop in photoyield was due to disruption of the activation layer and how much was due to atomic dislocations in the photoemitting crystal lattice. These results appear in figure 36, together with the change as seen using the standard procedure of activation followed by ion bombardment. The two damage contours are similar, but there was a higher drop (down to ~0) for the Xe dosed activated surface at the beam centroid (left) as compared to the Xe dosed clean surface, which was subsequently activated (right). While some of the drop in the photoyield in the former case may be attributable to chemical reaction with the background gas composition as modified by the presence of the Xe in the chamber and the operation of the ion gun, the several percentage difference indicates that the damage was distributed throughout both the activation layer and the underlying GaAs. Hence, the more robust Cs+Li activation layer can, at best, only somewhat mitigate the ion effects when the flux, mass and energy of the ions are sufficient to penetrate and disrupt the underlying crystallinity.

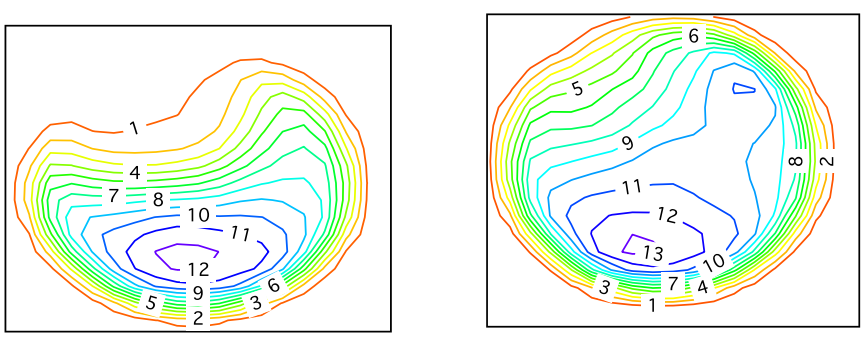

Figure 36. Contour plots showing the photoyield for a photocathode following 2 kV Xe ion dosing after (left) and before (right) Cs+NF_3 activation.

A compendium of the ion data measurement data parameters appears at the end of this report

(less the final hydrogen and xenon values). A user friendly version of the data is being compiled into a form suitable for publishing to make the data (reduced to the effect on photoyield at a particular wavelength, per ion as a function of ion species and energy + resultant enhancement in chemical degradation) available as soon as possible to the accelerator community since this report will not become publicly available for several years. The intended journal for publication is Phys. Rev. ST Accel. Beams.

Task 8: Electron stimulated recovery current and energy measurements

Recommissioning of the second system involved activation of GaAs (100 nm MBE grown) with Cs and Cs+Li in order to determine the correct Li source current for optimal bi-alkali activations. Other recommissioning activities included setup of the lifetime monitoring system, software control of same and extensive, long term outgassing of the electron gun currently in use. Photoyield data taken for Cs and Cs+Li activated samples are shown in figure 37. Rejuvenation data taken to date have all been from Cs activated surfaces. An example of a rejuvenation cycle (with spatially averaged response) is shown in figure 38. The sample was activated on the first day, then peaked up with Cs on the second. Lifetime was then monitored as described in ref. 2 for ~20 minutes to establish a baseline for the photoemission decay. CO_2 dosing began at $2x10^{-10}$ Torr over base pressure. When the photoyield had decayed, the electron gun was turned up to generate > 20 μA secondary electron current (sample biased negative). When an inflection was reached, the CO_2 was stopped with the electron beam ceased at the next inflection. The behavior is somewhat different than in the other two chambers (see below).

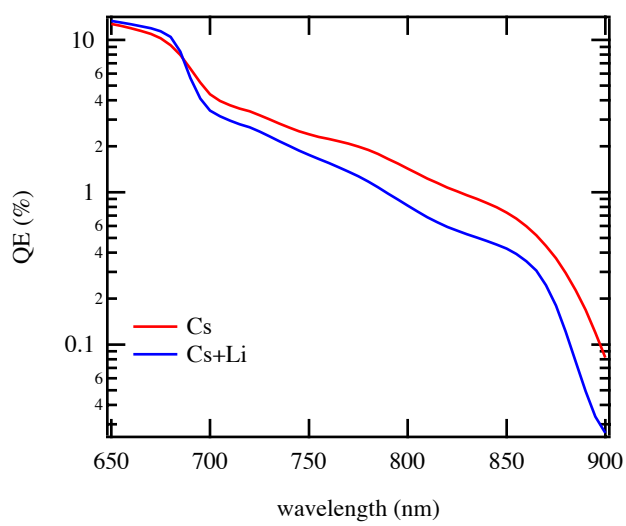

Figure 37. Photoyield versus wavelength of Cs and Cs + Li activated 100 nm MBE grown GaAs acquired as part of chamber commissioning tests.

These results allowed the following semi–quantitative statements to be made:

1. Electron beam energies in the 2 to 3 kV range at a secondary current greater than 20 μA have about the same effect. This is not too unexpected since the electron mean free path ('universal' curve) shows little change in penetration depth in this range. Lower energies should show greater variation. These measurements were all conducted with the electron beam (nearly) filling the

sample, which equates to a secondary electron current density of 0.3 μA/mm^2. Complete rejuvenation seems to require the presence of a CO_2 overpressure, though another oxygen bearing gas may serve as well.

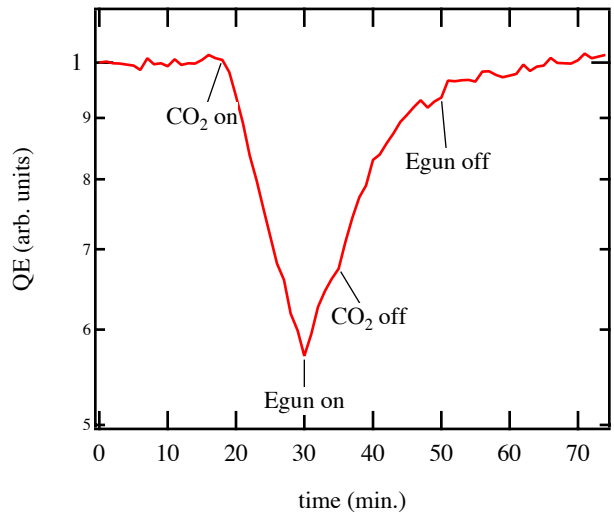

Figure 38. Electron beam induced quantum efficiency recovery of bulk GaAs following dosing with CO_2.

2. In two of the four systems in which the rejuvenation effect has been demonstrated, the secondary current required was different by one order of magnitude than in the other two. There are two possibilities with greatest likelyhood. In the initial tests in chamber 1 during the Phase I, the secondary electron current dependency was explored in a very limited fashion. Lower secondary electron currents than the one finally settled upon resulted in a diminished rejuvenation rate, but the effect was still present. In the recommissioning of chamber 2, very low secondary electron currents were tried, but did not result in rejuvenation, rather it resulted in a decrease in photocurrent. This may be in part due to competition between CO_2 devolving from the gun and the electron stimulated desorption, which is the clear mechanism (see below) for the rejuvenation. The same electron gun was used in both those chambers. In the demonstration chamber, constructed of 2-3/4" CF hardware, the internal volume was small and the chamber walls were in very close proximity to the sample. In the SSRL end station, the volume surrounding the sample was also crowded. In each of those systems, the required secondary electron current was low (~1 μA). In the demonstration system, attempts to utilize higher secondary electron currents resulted in a decreasing photoyield. Both the demonstration system and the SSRL end station utilized the same manufacture and model gun, though not the same gun. Those guns were equipped with thoriated iridium filaments. The proximity of the chamber walls and surfaces of the analysis tools to the sample suggests that ancillary desorption placed a limit on the secondary current (through limiting the primary current), while the lower gas (CO_2) generation rate of the thoriated iridium filament suggests that operating at higher secondary electron currents enables a process to occur that, if not mediated by a CO_2 overpressure, was debilitating to the photoemitter.

The apparatus for acquiring the electron beam profiles was described earlier. For beam

positioning and focussing, it was found to be most efficient to install via loadlock a phosphor screen in place of the photocathode rather than to use the profile arm to locate the beam (along one axis only). Once the beam size and the position were set, the actual profile data were acquired. An example data set appears in figure 39. Beam profiles are generated by differentiating these integral data. Care must be taken, however, as along some regions of the profiler, the arm gaps are small enough that they act more like Kronecker delta functions than as semi-infinite plates. Those regions yield the beam profile directly, rather than an integral of the beam. From the data, it is clear the beam widths are only a few mm FWHM for the small and large beam cases. In either event, the beam profile often becomes directly inferable from the photoyield as monitored by the improved data acquisition software.

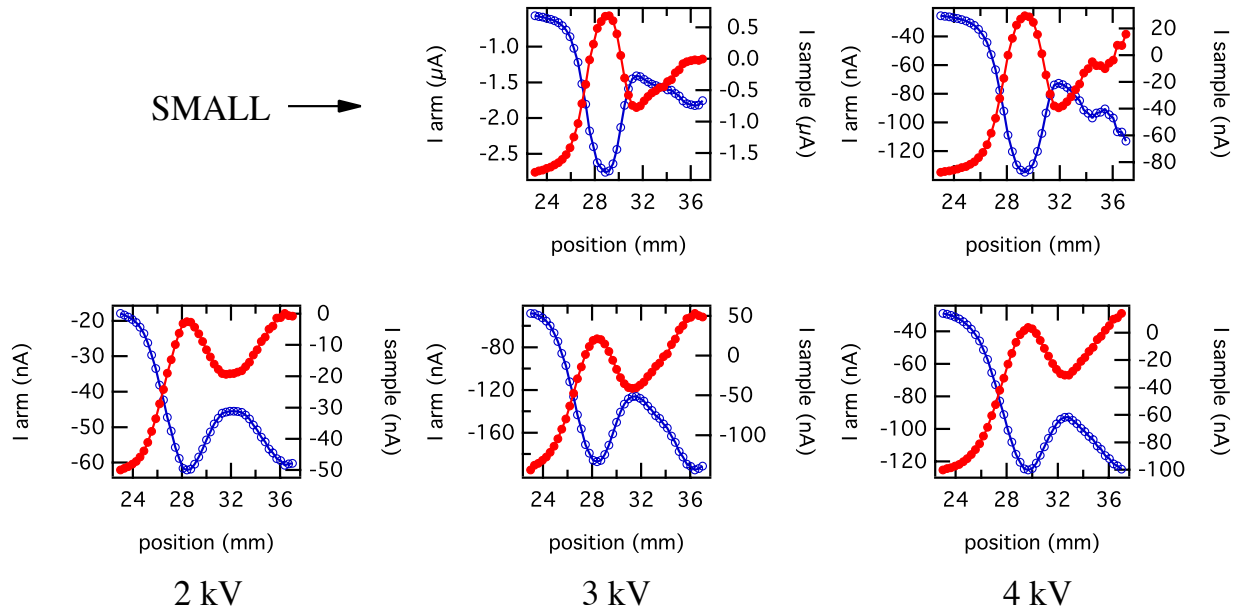

Figure 39. Electron beam profile data acquired by motion of the beam profiler for various energies. Current was collected on the arm and on the sample. Smaller beams appear on the upper row and larger beams on the lower row.

Our two types of photoyield monitoring code, spatial mapping and ESR single point value, were combined to provide a better method for measuring the photoyield during the ESR process. The mapping software was converted to take the signal from a lockin amplifier (as for the ESR single point value code) rather than the direct current as measured by a picoammeter. The code was further modified to determine the maximum photoyield value and plot that value in real time as each array of photoyield data is acquired. All data are stored: the maximum versus time as one file and each photoyield map as an independent file. Upon joining, the map files provide a time-lapse movie illustrating the photoyield over the ESR process. Electron beam profiles can be directly visualized by the beam's action upon the photoyield. This new method allows direct monitoring of the secondary electron current combined with the photocurrent as in the previous code, permitting the dependence of the ESR on primary beam current to be measured while obviating the need to provide a photoyield monitor beam exactly coincident with the ESR beam. An example of the photoyield as a function of time is shown in figure 40 for a 3 kV ESR beam.

Following CO_2 exposure and ESR, the photocathode's maximum QE had returned to approximately its starting value, first in the centroid of the electron beam, then over most of the photoemitter. The photoyield sequence as contour plots is shown in figure 41 for the starting condition (left), midway through recovery (middle) and at the end (right).

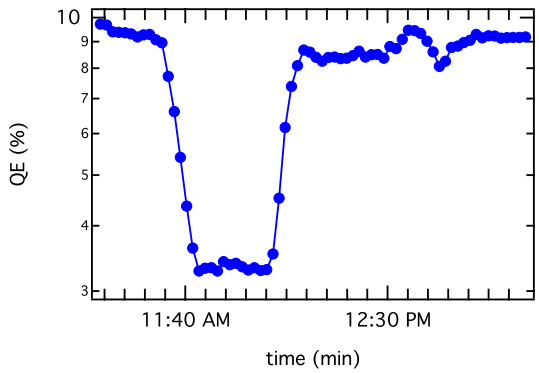

Figure 40. Photoyield as a function of time as acquired with the new software. The photocathode was first monitored for background induced decay, exposed to CO_2 to drop its photoyield, monitored for background induced decay, exposed to an electron beam for ESR, then lastly, with both CO_2 and electron beam off, monitored for background induced decay.

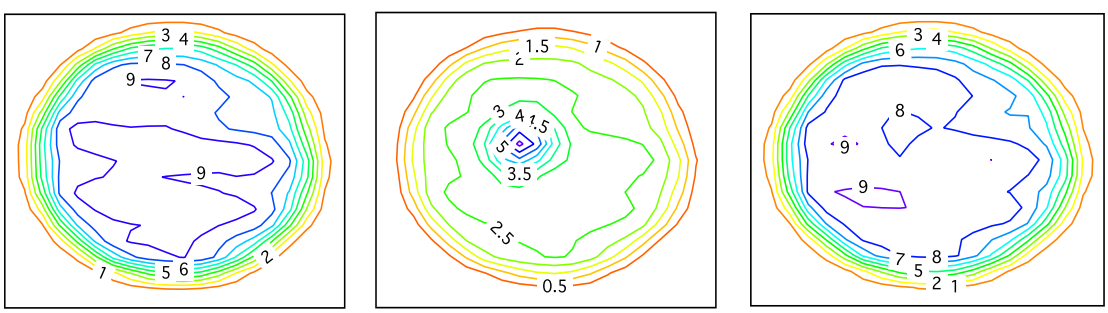

Figure 41. Photoyield sequence during the ESR sequence as contour plots for the starting condition (left), midway through recovery (middle) and at the end (right).

The results for energy and flux dependence for ESR on Cs and Cs + Li activated GaAs photoemitters may summarized as follows:

- Little to no energy dependence for 1.5 to 5 kV primary beam energies,
- Little to no dependence, but for rate, for primary beam currents over 2 orders of magnitude and
- ESR is effective on both Cs and Cs + Li activated GaAs.

While the electron beam energies explored so far did not yield any major difference in behavior, this is likely due to the relatively small difference in the electron penetration depth and thereby, secondary electron yield. It is expected that at the lower energies possible in the chamber with the mu-metal shielded low energy electron gun (see below), any significant changes in rate not

related to primary beam current will become apparent.

In the course of observing the ESR process with the new monitoring code, it became very apparent that the sequence employed could be used for writing electron emission patterns to the photocathode. A few possibilities are shown in figure 42. The leftmost pattern as a real profile is shown in figure 41 (middle), though as a top view. We deliberately generated the middle pattern of figure 42 on a photocathode with the result shown in figure 43. The asymmetries in the peak amplitudes are due to both the manual technique used to move and 'park' the electron beam at the four cardinal points and the response of the photocathode. These shortcomings can be fixed by more rapidly scanning the photocathode and parking the beam longer on the points needing adjustment, all under computer control. Applications for this technique include off-axis emission in injector sources, electron beam lithography and shaped beams for other specialized applications.

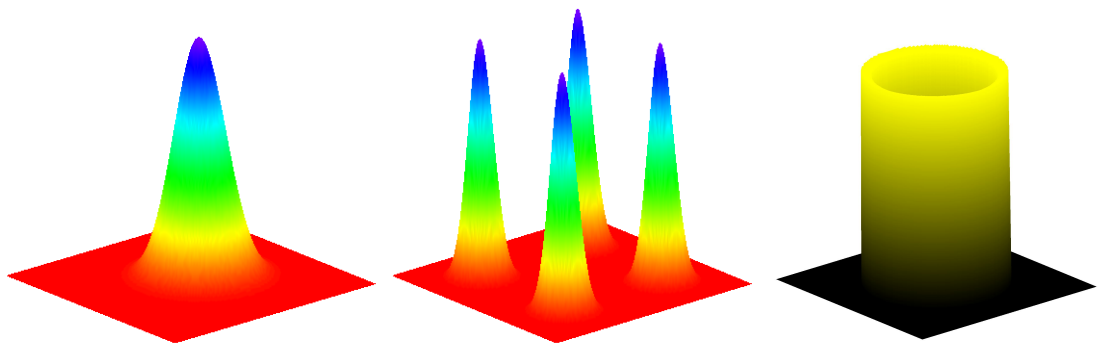

Figure 42. Examples of simulated electron beam emission profiles that can be tailored *in situ* by writing the desired shape with an auxiliary electron beam source following photoyield leveling with an oxidizing gas. These include off axis (left), multiple beams (center) and hollow beam (right).

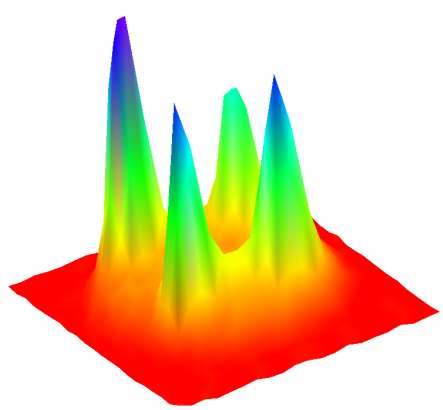

Figure 43. Actual four beam electron beam emission profile written with an auxiliary electron beam source following photoyield leveling via CO_2 exposure.

The retarding field measurement system setup is shown in figure 44. The support hardware

(loadlock, sample transfer, etc.) are clones of those employed in chamber #3 as described below. A four grid Perkin-Elmer model 15-120 LEED-Auger optics set was used as both the low energy electron source and as the retarding field analyzer of the secondary electrons.

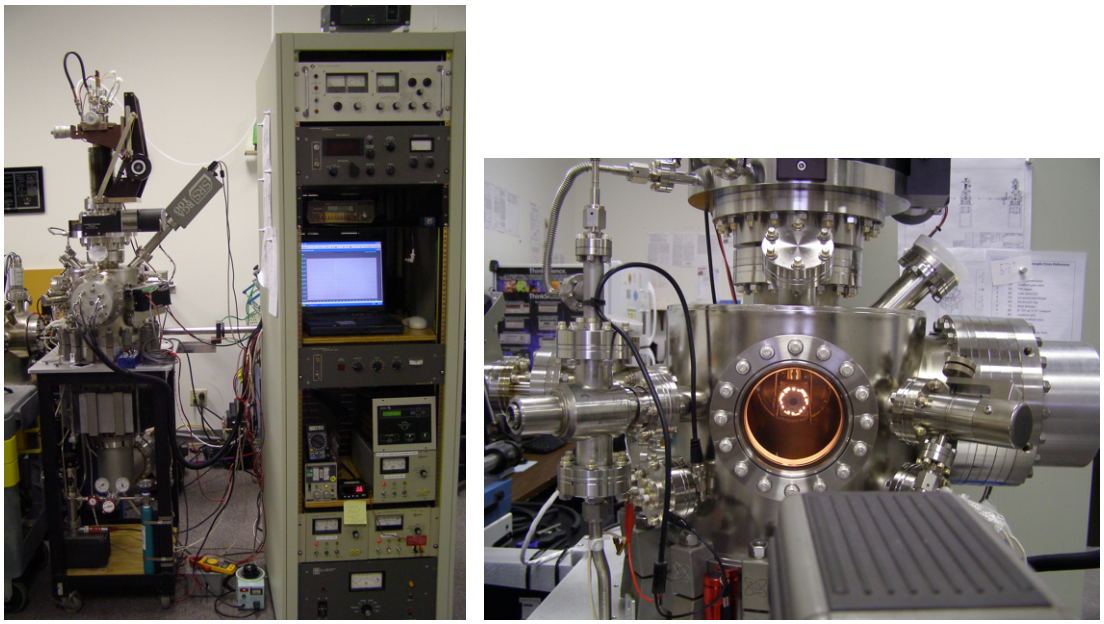

Figure 44. Chamber 4 photocathode test system (LEED optics end view) plus electronics control rack (left photo) and close up of system while photocathode was being heat cleaned (right photo; left side view of system in other photo).

The low energy electron gun as part of the retarding field analyzer (LEED optics) is shown in figure 45. This gun was used as the electron source for ESR since it has a very well controlled output over a large energy range and can operate at rather low energies (100 V as lower limit in this case) compared to the Perkin-Elmer gun used in the original work. The retarding field analyzer consists of concentric spherical sections covering 120°. The first grid, G1, which faces the sample, is kept grounded to provide a (mostly) fieldfree region when used for LEED applications. In our case, G1, was kept at ground potential through an externally shorting MHV connector. G2 and G3 are ordinarily used for energy discrimination: in LEED to suppress the background; in Auger measurements to analyze portions of the electron energy distribution. For measurements of the total secondary electron yield, we once again grounded the two grids with an external MHV shorting connector. These two grids are connected together internally. The collector, a solid spherical section coated with a phosphor, was used to collect the electron current passing through the three semi–transparent grids. The grid have an electron transparency of approximately 80%, so with three grids in total, the current incident upon the first grid is attenuated by 0.8^3, or ~ 50% by the time it reaches the collector. For the purpose of measuring the electron current, the collector was always biased 100 V greater than the primary electron beam as measured by the gun voltage. This insured that all primary and secondary electrons incident on the collector were captured.

The secondary electron yield, defined as the ratio of the emitted electron current divided by the incident electron current, was determined in two ways. First, the sample was biased by -76 V to

insure that all electron current left the sample, both primary and secondary electrons. The current was the measured both leaving the sample and as collected by the LEED optics. These data are shown in figure 46 as a function of gun voltage (energy). Note that the beam energy with respect to the sample is shifted from the gun value by the bias. The current values are rather linear with gun energy, with some small deviation from linearity at the lowest energies. The ratios of the slopes is exactly 2, consistent with 100% capture of the electron current into the LEED optics followed by 50% transmission to the collector.

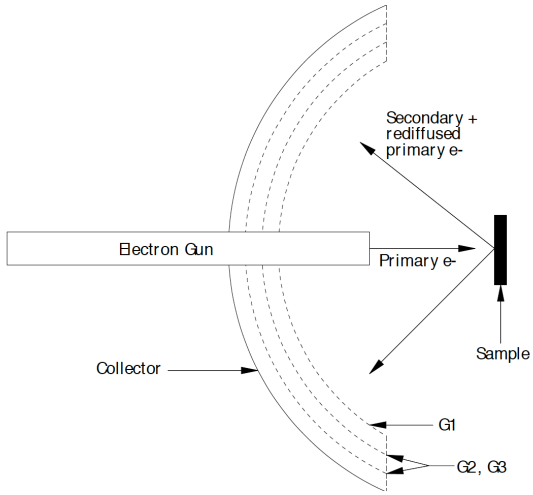

Figure 45. Schematic of 120° retarding field optics comprised of grids (G1, G2 and G3) and a solid collector (phosphor screen) with coaxial low energy electron gun. G2 and G3 are internally tied together to provide uniform energy discrimination. Drawing is not to scale.

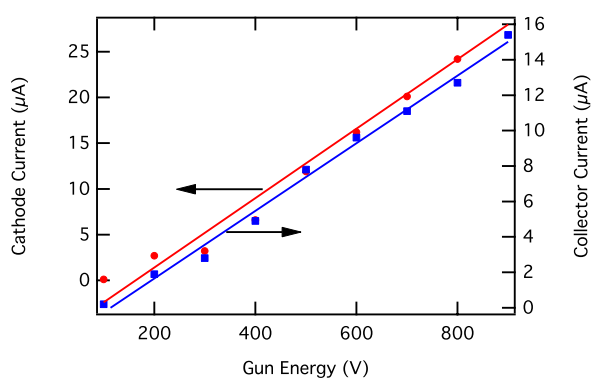

Figure 46. Total electron current leaving the sample (cathode current) and as captured on the collector (collector current) after passing the retarding field grids (G1, G2 and G3 all at ground potential).

It is necessary to accurately measure the primary electron current so that the ratio of currents can be obtained. This was done by biasing the sample positively so that the secondary electrons, which comprise the majority of the current (the elastic electrons are only a few percent of the complete electron distribution), while allowing the elastically scattered and/or rediffused primary

electrons to escape. The distributions, as a function of electron gun voltage are shown in figure 47. The distribution shape does not change with the sample bias indicating that the current output of the gun is set by the gun bias (as it should be!) and is not influenced by the sample potential. The relative shifts in the total current with bias are less than 10%.

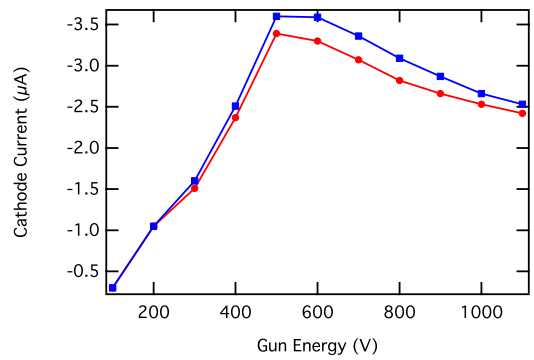

Figure 47. Primary electron current as collected on the cathode with a positive bias of 324 V (red) and 76 V (blue). The maximum relative difference is < 10%.

The secondary electron yield was obtained by both subtraction out the primary electron beam and by leaving it in the total collected current before dividing by the primary beam current. Both results are shown in figure 48. The curves are necessarily displaced from each other, but the overall shift, except at the lowest energies, is a large value, relatively. At the lowest energies, however, the values are rather more uncertain. Fits to the curves using a simple second order polynomial are also shown. Extrapolation to higher energies for purposes of comparing the secondary electron yield to direct measurements made in the kV range, remarkably results in nearly the same value as obtained in that fashion (yield ~ 50 at 2 kV). Clearly if the ESR process is dependent on the quantity of electrons transported across the activation layer, then the higher primary electron energies are the most desirable ones to be used, in keeping with observations.

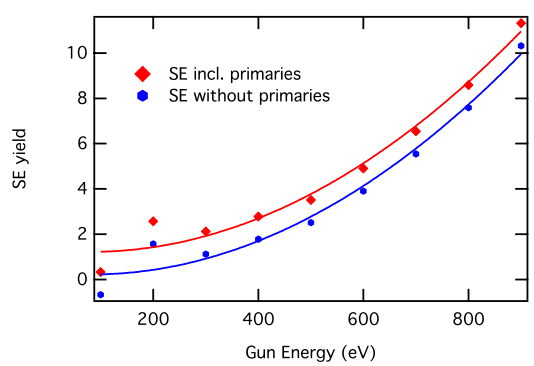

Figure 48. Secondary electron yield as a function of the gun energy calculated with (red) and without (blue) the contribution of the primary electrons (figure 47) to the total current (figure 46). The fits are second order polynomials. Extrapolation to the 2 kV beam energy used in previous measurements give a SE yield of ~50, consistent with the measured values at higher beam energies.

Task 9: Acquire ESD dedicated quadrupole mass analyzer and prep chamber

Receipt of the Hiden IDP probe and associated electronics occurred on November 30, 2011. The unit was installed into the chamber once the final shakedown tests occurred. The Hiden software was installed onto the computer which was used for DAQ control.

Assembly drawings of the electron stimulated desorption (ESD) during ESR measurement system (chamber #3) are shown in figures 49-51. Installation, sensitivity checkout by Xe for high mass and K+ ions from the W heater of the sample holder was followed by a system bake. The system is equipped with stand-alone two electron guns both for redundancy and for the different incident angles they cover. The Kimball Physics EFG-7 gun is near to normal to the sample, while the Perkin-Elmer 04-015 is at nearly 45° to the sample surface. Both can be used with the quadrupole for ESR. A near-normal viewport allows light access to the sample at the ESR position. The system is loadlocked with a newly-designed vertical sample holder (based on old, proven designs from the literature) to allow access to the sample surface by the preexisting ports on the chamber. A low energy electron gun will be included, though it cannot be accessed at the same position as provides direct access to the quadrupole. The actual assembled system is shown in figure 52.

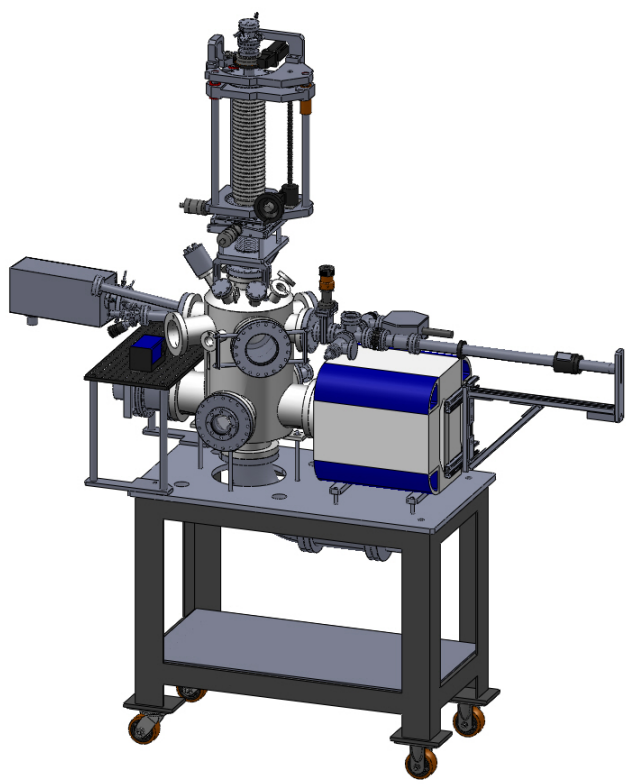

Figure 49. Perspective view of the new system incorporating the Hiden IDP quadrupole mass spectrometer (far left) for molecular fragment measurements during the electron stimulated recovery process.

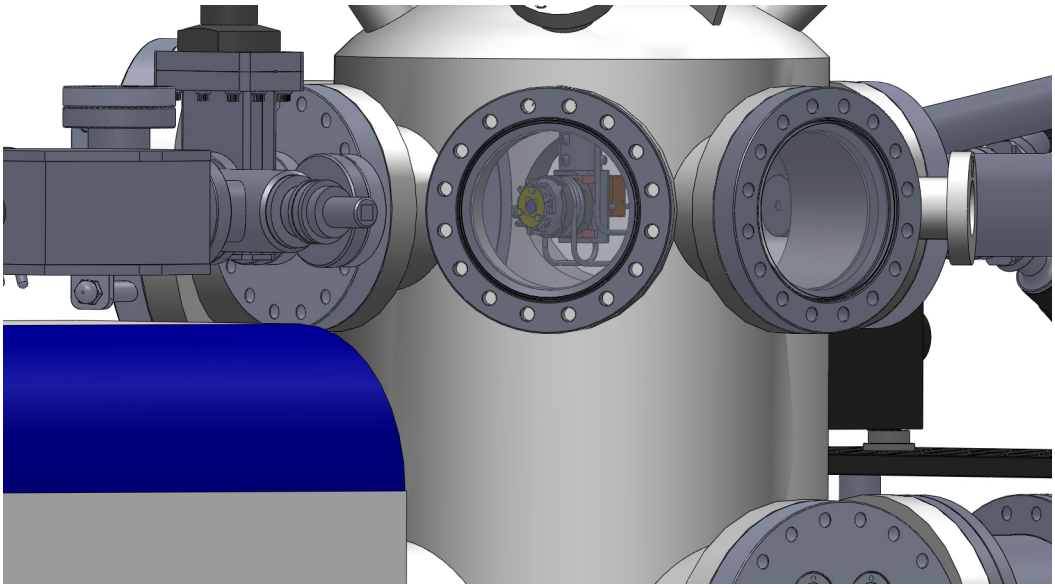

Figure 50. Intermediate distance view of the sample holder in the new system with the mass spectrometer to the far right and the loadlock to the left. The sample holder is visible through the left viewport.

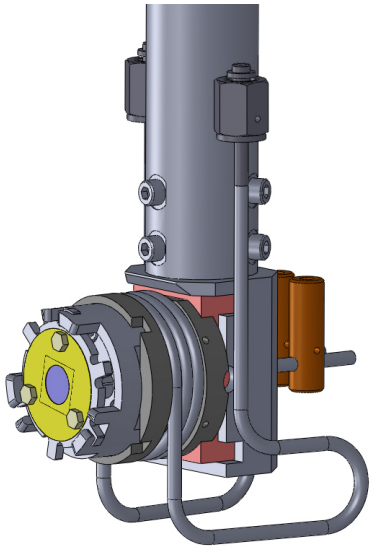

Figure 51. Closeup view of the sample holder showing the cooling lines and sample dock details. The clamping disk (yellow) is tantalum, while the securing screws (white) are alumina. The cooling and filament electric power lines are shown unconnected.

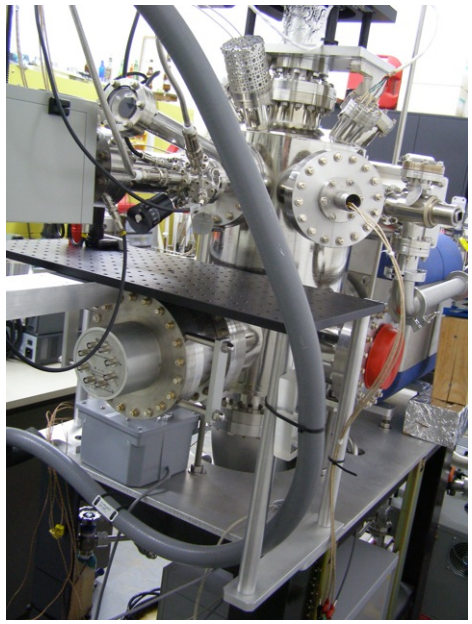

Figure 52. Side view of Chamber 3 from spectrometer/electron gun(s) end. The spectrometer is attached to the large RF generator box powered through the grey umbilical by the control unit under the chamber table. The electron gun flange is just below the viewport in the upper left corner of the photo. The 400 l/s ion pump (blue) is visible to the far right.

The Hiden IDP (low energy option) mass spectrometer with HAL 7 controller was subject to extensive characterization and testing before performing any ESR related measurements. Prior to bakeout (and post bake) the spectrometer's mass analysis calibration and sensitivity in residual gas analysis (RGA) mode was tested by admitting Xe gas via a leak valve. Xe was chosen as it has high mass peaks and would be cleanly pumped away, unlike the hydrocarbon gas used at Hiden for their pre–sale testing. The results of such a test are shown in figure 53. The manifold of Xe peaks are clearly visible superimposed atop the background appearing at each mass increment. The Xe isotopes [3] at 128, 129, 130, 131, 132, 134 and 136 amu were all observed at the correct charge to mass ratio with the natural abundance ratios.

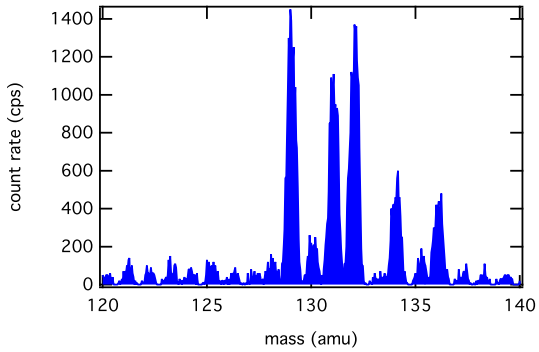

Figure 53. RGA scan of Xe gas used to verify mass alignment of the spectrometer and sensitivity at high mass.

Additional characterization was performed to insure the incident ion detection features functioned as expected. The requires the spectrometer to be run in the "SIMS" mode so that the ionizer used for RGA analysis (to detect neutrals) is inactive. Data were taken on the species emitted by an apertured tungsten filament at elevated temperature. The aperture was to insure a nearly point–like source. It is well known that very small, but measurable amounts of positive alkali ions are emitted from tungsten filaments at elevated temperatures. Data taken for three such ions, K, Na and Rb are shown in figure 54. Each appears at the expected mass value and with the natural isotopic abundance ratio.

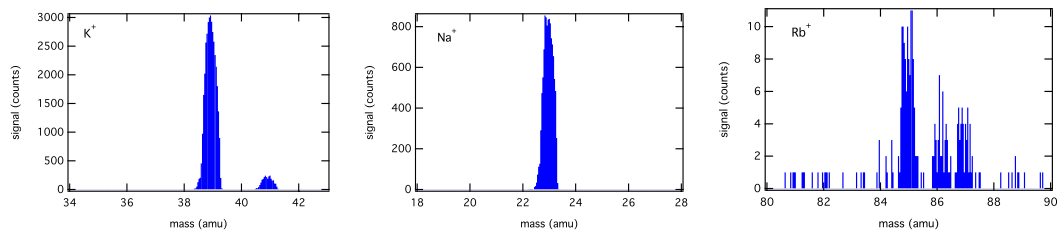

Figure 54. Alkali positive ion signals (K, left, Na, center and Rb, right) obtained from a hot tungsten filament.

Alignment of the electron beam was set by insertion of a Kimball-Physics P22 phosphor screen in place of the photocathode sample holder. A picture of the electron beam at 1 kV is shown in figure 55. This alignment was performed both pre– and post–bake with very little difference in position observed between the two cases. This provides a great deal of certainty that the alignment is preserved between sample measurements as well, i.e., the electron beam is incident upon the photocathode and not the tantalum clamping disk. For more verification of the proper operation of the spectrometer, ion data (non–neutral), was acquired and is shown in figure 56.. Electron beam induced phosphor degradation is a large issue for display technology (see, e.g., ref[4]). Known decomposition fragments, such as Al and Cl are observed at masses 27 and 35/37, respectively. Most prevalent in all these spectra is H, which is simply a result of its solubility (or void filling as a gas) in most materials.

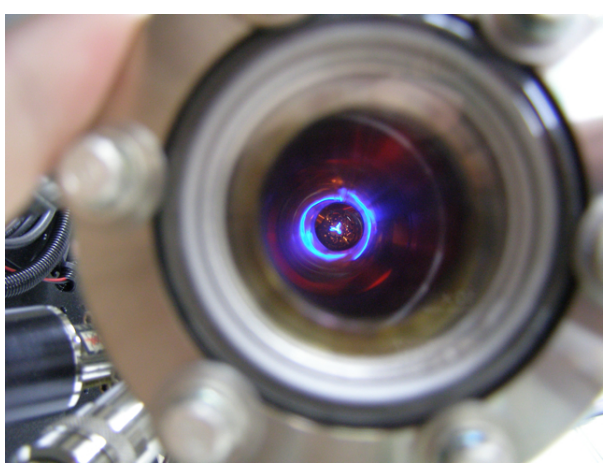

Figure 55. Alignment of the Kimball Physics electron gun beam (three-lobed blue image in center of photo) using a phosphor screen inserted in place of the sample.

This electron gun is designed for small spot generation, hence the unusual pattern for the expanded beam. The beam lobes were set to cover the entire exposed sample surface during the ESD measurements. The blue circle is due to reflected light.

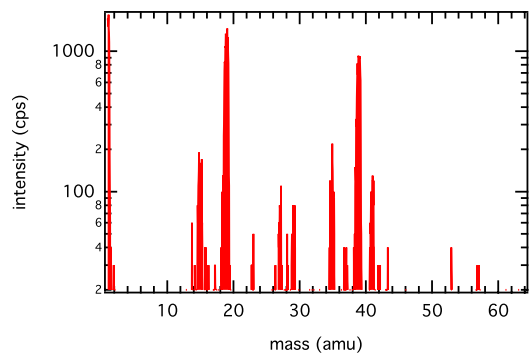

Figure 56. ESD spectrum of positive ions summed over three scans taken from the P22 phosphor plate using electron beam energies ranging from 500 to 1,500 V. The full scan range was 200 amu, but only that portion of the plot showing any features is shown.

Task 10: ESD measurements of electron stimulated photocathodes

Photocathode decay and ESR processes where the next processes investigated. In the following figure, 57, the positive ion spectrum due to electron beam (nominal 1 kV) impact is displayed. The spectrum showed very little activity, with only atomic hydrogen (H_1) and atomic fluorine (F_1) in evidence. These data were from an 'healthy' photocathode, i.e, one that had not decayed due to either background gas interaction or by deliberate gas exposure.

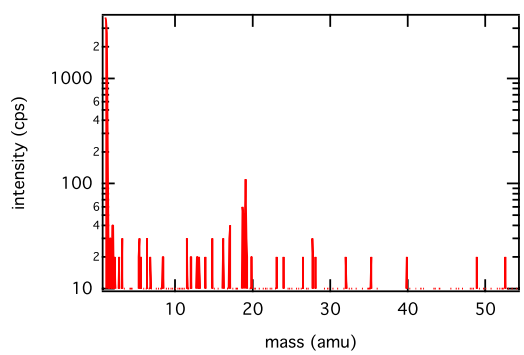

Figure 57. ESD spectrum of positive ions summed over the first 4 scans for a sample with a high QE diminished by overcesiation. Clear (1 amu width) peaks are visible for, in order of descending intensity, H_1 and F_1. The other 'peaks' are too sparsely populated in width to be considered real. A scan to higher mass (200 amu) did not reveal any additional species.

In a contrasting test sequence, the photocathode was made to purposely decay by the application of CO_2 until the photoyield was reduced by a factor of 10 from its starting value. The positive ion spectrum generated by the action of a 1 kV electron beam on that surface is shown in figure 58. In this case, several new peaks came into being and the ratio of the F_1 to H_1 peaks changed

dramatically, i.e., there was a greater proportion of F_1 than before. It is clear that the surface which had decayed through absorption of CO_2 was rejuvenated by the cracking and ejection of both the various subspecies due to the absorption of CO_2 and some of the F_1, which apparently the absorbed (via disassociation) O_1 displaced. Thus, the emergency of greater rates of F and the presence of O_2 and CO during the electron beam treatment of the decayed surface. This is entirely consistent with the photoemission data discussed earlier. However, the signal strengths are much greater, so the desorption products can be identified with much greater certainty. No indication of alkali desorption was seen in any of the spectra taken from an activated surface. The presence of a large O_2 peak counter indicates any contribution from residual gas phase CO_2 to the spectrum.

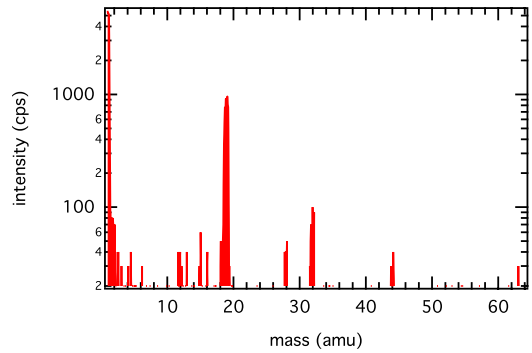

Figure 58. ESD spectrum of positive ions summed over the first 6 scans for a sample with the QE dropped by one order of magnitude via CO_2 exposure. With a dwell time of 100 ms per point, the cumulative rate represents 0.6 s total dwell time. Clear (1 amu width) peaks are visible for, in order of descending intensity, H_1, F_1, O_2, H_2, and possibly CO and C_1. The other 'peaks' are too sparsely populated to be considered real.

In contrast, the negative ion spectrum, figure 59, very much dominated by the electron background, only showed a strong signal by H_2, with not other species being readily identifiable, either directly or through signal differentiation.

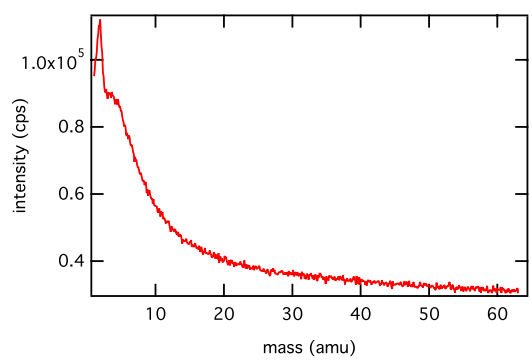

Figure 59. ESD spectrum of negative ions. With the electron gun as an excitation source, there is a vast background of secondary electrons overlaying most of the ion signal. The only negative ion apparent by inspection is at 2 amu (H_2). Differentiation did not reveal any other peaks hidden by the in the spectrum over the range shown, though that could be due to insufficient amplitude (see the positive ion spectrum).

Milestone Schedule

The two year program schedule is reproduced below.

Year 1 First 6 months

Month	1	2	3	4	5	6
Design and fab chamber 1 mods						
Install flange, ion gun, gas, etc.						
Bake and recommission						
Commence ion studies						
Design and fab chamber 2 mods						
Install flange, egun, gas, etc.						
Bake and recommission						

Year 1 Second 6 months

Month	7	8	9	10	11	12
Commence ebeam studies						
Continue ion studies						
Modify training system for SSRL						
REK training at Saxet						
Setup training system at SSRL						
XPS at SSRL						

Year 2 First 6 months

Month	1	2	3	4	5	6
Continue ebeam measurements						
Continue ion measurements						
Acquire quadrupole						
Prep system for quadrupole						
Commence ESD measurements						
Setup ret. field msmt. system						

Year 2 Second 6 months

Month	7	8	9	10	11	12
Continue ESD measurements						
SE yield measurements						
Final Report						

Sample of Ion Data Acquisition Parameter Database

Date	Cathode type	Cs/Cs+Li	Heat clean #	I max (nA)	Opt. Pwr. (uW)	Wavelength (nm)	QE %	Peak-up %	Dosing gas	Dosing press. (Torr)	Dosing time (min.)	Energy (kV)	Battery/Sample	Beam I(uA) METER Start	Beam I (uA) METER Stop	Beam I (uA) NEG	Beam I (uA) POS	CO2 dosings	Time min.	Notes
1/24/11	Wafertech 35	Cs	1	670	8.76	633	15	8.6					Negative							Activation on new sample prior to the ITT visit.
1/28/11	Wafertech 35	Cs+Li	2	710	9.3	633	15	8.2					Negative							CS + Li activation for ITT demonstration. CO2 exposures 2 days later.
2/2/11													Negative					4	2/5 2/10	CO2 dosing was done in two stages, 5 and 10 minute.
2/5/11	Wafertech 35	Cs	3	690	9.23	633	14.6	8.9					Negative							Cs activation for CO2 dosing experiments only.
2/7/11													N/A					4	2/5 2/10	CO2 dosing was done in two stages, 5 and 10 minute.
2/8/11	Wafertech 35	Cs	4	680	9.83	633	14.1	10.7					Negative							
2/9/11									Ar	4.00E-09	10	1	Positive	1.19				4	2/5 2/10	CO2 dosing was done in two stages, 5 and 10 minute.
2/10/11	Wafertech 35	N/A	5	N/A	N/A	N/A	N/A	N/A					N/A							
										4.00E-09	N/A	Assorted	N/A							Heat clean only, no activation. For ion beam profile data.
2/16/11	Wafertech 35	Cs+Li	6	840	9.57	633	18.2	15					Negative							
2/17/11									Ar	4.00E-09	10	1	Positive	1.3	2.4			4	2/5 2/10	CO2 dosing was done in two stages, 5 and 10 minute.
2/23/11	Wafertech 35	Cs	7	810	9.57	633	16.6	11.3					Negative							
2/24/11									Ar	4.00E-09	10	2	Positive				1.9 1.1	4	2/5 2/10	CO2 dosing was done in two stages, 5 and 10 minute.
2/25/11	Wafertech 35	Cs+Li	8	870	9.29	633	18.3	14.3					Negative							
2/26/11									Ar	4.00E-09	10	2	Positive	1.8	1.85			4	2/5 2/10	CO2 dosing was done in two stages, 5 and 10 minute.
2/28/11	Wafertech 35	Cs	9	770	10	633	15.1	11.9												
3/1/11									Ar	4.00E-09	10	0.5		1.17				4	2/5 2/10	CO2 dosing was done in two stages, 5 and 10 minute.
3/2/11	Wafertech 35	Cs+Li	10	880	9.34	633	18.4	14												
3/3/11									Ar	4.00E-09	10	0.5		1.56nA				4	2/5 2/10	CO2 dosing was done in two stages, 5 and 10 minute.
5/2/11	Wafertech 39	Cs	1	820	9.65	633	16.6	12.3					Negative							
5/3/11									Ne	4.00E-09	10	2		0.66	1.56	0.59nA		4	2/5 2/10	CO2 dosing was done in two stages, 5 and 10 minute.
5/4/11	Wafertech 39	Cs	2	790	9.25	633	16.7	12.3					Negative							
5/5/11									Ne	4.00E-09	10	1.3	Negative			1.5 N/A		4	2/5 2/10	CO2 dosing was done in two stages, 5 and 10 minute.
5/6/11	Wafertech 39	N/A	3	N/A	N/A	N/A	N/A	N/A	Ne	4.00E-09	N/A	N/A	N/A	N/A	N/A	N/A	N/A	N/A	N/A	Heat clean only to perform ion beam profiles, all energies.
5/9/11	Wafertech 39	Cs	4	890	9.42	633	18.5	13.3					Negative							
5/10/11									Ne	4.00E-09	10	0	Negative	4.28nA			-0.945	6	5	All CO2 dosing done at 2.0E-10 Torr over base pressure.
5/11/11	Wafertech 39	Cs	5	720	9.22	633	15.3	11.9					Negative							
5/12/11									Ne	4.00E-09	10	0.5	Negative	1.5				6	5	All CO2 dosing done at 2.0E-10 Torr over base pressure.
5/13/11	Wafertech 39	Cs	6	720	9.41	633	15	11.7					Negative							
5/14/11									Ne	4.00E-09	10	2	Negative	1.2			0.38	6	5	All CO2 dosing done at 2.0E-10 Torr over base pressure.
5/17/11	Wafertech 39	Cs	8	810	8.75	633	18.1	12.7	N/A	3.60E-10		2	Negative	1.1	1.06	0.395nA				Ion beam currents only, no gas in system except background gas.
5/19/11	Wafertech 39	N/A	9	N/A	N/A	N/A	N/A	N/A	N/A	N/A	N/A	N/A	N/A	N/A	N/A	N/A	N/A	N/A	N/A	Heat clean only to measure ion currents.
5/27/11									Ne	4.00E-08		2	Negative	7.6nA	(-)7.6nA	(-)1.1nA				Ne ion currents on sample. Ne partial pressure (RGA) 6.4E-9 Torr.
									Ne	4.00E-08		1.5	Negative	5.3nA	5.8nA	0.52nA				RGA and ion gauge filaments off during measurements.
									Ne	4.00E-08		1	Negative	4.1nA	5nA	(-)0.9nA				
									Ne	4.00E-08		0.5	Negative	3nA	4nA	(-)2.6nA				
									Ne	4.00E-08		1.5	Negative	4.9nA	5.6nA	(-)10.2nA				
									Ne	4.00E-08		2	Negative	5.6nA	6.3nA	(-)10.5nA				
5/30/11	Wafertech 39	Cs	1	690	9.13	633	14.8	9.8					Negative							
5/31/11									Ne	4.00E-08	1+6sec.	2	Negative	1.1	0.7			6	5	All CO2 dosing done at 2.0E-10 Torr over base pressure.
6/1/11	Wafertech 39	Cs	2	630	9.15	633	13.5	12.1					Negative							
6/2/11									Ne	4.00E-08	1+9sec.	0.5	Negative	1.3				6	5	All CO2 dosing done at 2.0E-10 Torr over base pressure.
6/3/11	Wafertech 39	Cs	3	720	9.19	633	15.3	10.5					Negative							
6/4/11									Ne	4.00E-08		1	Negative	1.3	0.91			6	5	All CO2 dosing done at 2.0E-10 Torr over base pressure.
6/6/11	Wafertech 39	Cs+Li	4	810	988	633	16	16.5					Negative							
6/7/11									Ne	4.00E-08	1+6sec.	2	Negative	1.7	1.2			6	5	All CO2 dosing done at 2.0E-10 Torr over base pressure.
6/8/11	Wafertech 39	Cs+Li	5	790	9.18	633	16.8	13.4					Negative							
6/9/11									Ne	4.00E-08	1+9sec.	0.5	Negative	1.7	1.4			6	5	All CO2 dosing done at 2.0E-10 Torr over base pressure.
6/10/11	Wafertech 39	Cs+Li	6	790	9.04	633	17.1	15					Negative							
6/11/11									Ne	4.00E-08	1+6sec.	0	Negative	33nA	35nA			6	5	All CO2 dosing done at 2.0E-10 Torr over base pressure.
6/13/11	Wafertech 39	Cs+Li	7	790	9.61	633	16.1	12.6					Negative							
6/14/11									Ne	4.00E-08	1+9sec.	1	Negative	1.9	1.4			6	5	All CO2 dosing done at 2.0E-10 Torr over base pressure.
6/15/11	Wafertech 39	Cs	8	N/A	N/A	N/A	N/A	N/A					Negative							
6/16/11									Ne	4.00E-08	N/A	0	Positive	N/A	N/A	N/A	N/A	N/A	N/A	Ion beam profiles only, no activation, no CO2 dosings.
6/22/11	Wafertech 39	Cs	9	690	9.06	633	14.4	9.9					Negative							
6/23/11									Kr	4.00E-08	1+9sec.	2	Negative	1.2	0.6			6	5	All CO2 dosing done at 2.0E-10 Torr over base pressure.
6/24/11	Wafertech 39	Cs	1	670	9.04	633	14.5	9.7					Negative							
6/25/11									Kr	4.00E-08	1+9sec.	1	Negative	1.2	0.71			6	5	All CO2 dosing done at 2.0E-10 Torr over base pressure.
6/27/11	Wafertech 39	Cs	2	700	8.73	633	15.7	10.8					Negative							
6/28/11									Kr	4.00E-08	1+9sec.	0.5	Negative	1.3	0.92			6	5	All CO2 dosing done at 2.0E-10 Torr over base pressure.
6/29/11	Wafertech 39	Cs+li	3	700	9.27	633	14.8	11.7					Negative							
6/30/11									Kr	4.00E-08	1+9sec.	2	Negative	1.7	1.137			6	5	All CO2 dosing done at 2.0E-10 Torr over base pressure.
7/4/11	Wafertech 39	Cs+Li	4	670	9.41	633	13.9	12.8					Negative							
7/5/11									Kr	4.00E-08	1+9sec.	1	Negative	1.7	1.2			6	5	All CO2 dosing done at 2.0E-10 Torr over base pressure.
7/6/11	Wafertech 39	Cs+Li	5	680	9.1	633	14.6	11.5					Negative							
7/7/11									Kr	4.00E-08	1+?	0.5	Negative	2.2	1.9			6	5	All CO2 dosing done at 2.0E-10 Torr over base pressure.
7/10/11	Wafertech 39	Cs	1	690	9.45	633	14.3	10.8					Negative							
7/11/11									Kr	4.00E-08	1+9sec.	2	Negative	1.3	0.7			6	5	All CO2 dosing done at 2.0E-10 Torr over base pressure.
7/13/11	Wafertech 39	N/A	2	N/A	N/A	N/A	N/A	N/A												
7/13/11									Kr	4.00E-08	N/A	0.5--2.0	Meter	N/A	N/A	N/A	N/A	N/A	N/A	Ion beam current profiles for Krypton
7/15/11	Wafertech 39	Cs	3	560	8.91	633	12.3	9					Negative							
7/16/11									Xe	4.00E-08	1+9sec.	2	Negative	1.03	0.5			6	5	All CO2 dosing done at 2.0E-10 Torr over base pressure.
7/18/11	Wafertech 39	Cs	4	600	9.39	633	12.5	9.1					Negative							
7/19/11									Xe	4.00E-08	1+9sec.	1	Negative	1	0.4			6	5	All CO2 dosing done at 2.0E-10 Torr over base pressure.
7/20/11	Wafertech 39	Cs	5	590	8.93	633	12.9	9					Negative							
7/21/11									Xe	4.00E-08	1+9sec.	0.5	Negative	1	0.7			6	5	All CO2 dosing done at 2.0E-10 Torr over base pressure.

7/22/11 7/23/11	Wallertech 39	Cs+Li	6	700	9.31	633	14.7	11.8	Xe	4.00E-08	1+9sec.	2	Negative Negative	1.05	0.7	6	5	All CO2 dosing done at 2.0E-10 Torr over base pressure.
7/25/11 7/26/11	Wallertech 39	Cs+Li	7	610	9.05	633	13.2	11.9	Xe	4.00E-08	1+9sec.	1	Negative Negative	1.05	0.7	6	5	All CO2 dosing done at 2.0E-10 Torr over base pressure.
7/27/11 7/28/11	Wallertech 39	Cs+Li	8	650	9.14	633	13.9	11	Xe	4.00E-08	1+9sec.	0.5	Negative Negative	1.3		6	5	All CO2 dosing done at 2.0E-10 Torr over base pressure.
8/1/11 8/2/11	Wallertech 39	Cs	9	590	9.08	633	12.7	N/A	Xe	4.00E-08	1+2sec.	2	Negative Negative	6 nA	5 nA	6	5	Sputter substrate before activation
8/2/11 8/4/11	Wallertech 39	N/A	10						Xe	4.00E-08								Ion beam profiles not current
8/2/11 8/5/11	Wallertech 39	N/A	10						Xe	4.00E-08		All						Ion beam current profiles
8/11/11 8/12/11	Wallertech 39	Cs	1	620	8.95	633	13.6	8.4	H2	4.00E-08	1+9sec/	2	Negative	1	0.7	6	5	First HF etched sample
8/15/11 8/16/11	Wallertech 39	Cs	2	580	9.08	633	12.5	9.1	H2	4.00E-08	1+9sec.	1	Negative	1.1	1	6	5	Standard dosing schedule
8/19/11 8/20/11	Wallertech 39	Cs	3	540	8.45	633	12.5	9.3	H2	4.00E-08	1+9sec.	0.5	Negative	1	1	6	5	Standard dosing schedule
8/23/11 8/24/11	Wallertech 39	Cs+Li	4	700	9.21	633	14.9	12	H2	4.00E-08	1+9sec.	2	Negative			6	5	Standard dosing schedule
8/25/11	Wallertech 39	Cs+Li	5															Bad activation Li on for too long during activation
8/26/11 8/27/11	Wallertech 39	Cs+Li	6	760	9.24	633	16.1	12	H2	4.00E-08	1+9sec.	1	Negative	1.6	1.5	6	5	Standard dosing schedule
8/29/11 8/30/11	Wallertech 39	Cs+Li	7	720	9.44	633	14.9	13.9	H2	4.00E-08	1+9sec.	0.5	Negative	1.5	1.4	6	5	Standard dosing schedule
8/31/11 9/5/11	Wallertech 39	N/A	8						H2	4.00E-08			No bias					Ion beam profiles not current
8/31/11 9/5/11	Wallertech 39	N/A	8						H2	4.00E-08			Positive					Ion beam current profiles
9/22/11 9/23/11	Wallertech 39	Cs	1	640	8.8	633	14.2	9.8	He	4.00E-08	1+8sec.	2		1.4	0.8	6	5	HF etched 10 min. 2% standard dosing schedule
9/26/11 9/27/11	Wallertech 39	Cs	2	590	9.26	622	12.48	10.4	He	4.00E-08	1+9sec.	1	Negative	1.3	1	6	5	Standard dosing schedule
9/30/11 10/1/11	Wallertech 39	Cs	3	590	8.86	633	13.04	11.07	He	4.00E-08	1+8sec.	0.5	Negative	1.2	1.1	6	5	Standard dosing schedule
10/5/11 10/6/11	Wallertech 39	Cs+Li	4	820	9.61	633	16.71	12.83	He	4.00E-08	1+9sec.	2	Negative	2	1.4	6	5	Standard dosing schedule
10/7/11 10/8/11	Wallertech 39	Cs+Li	5	780	9.34	633	16.36	14.23	He	4.00E-08	1+9sec.	1	Negative	1.9	1.6	6	5	Standard dosing schedule
10/11/11 10/12/11	Wallertech 39	Cs+Li	6	820	9	633	17.85	13.89	He	4.00E-08	1min.	0.5	Negative	1.8	1.7	6	5	Standard dosing schedule
10/13/11 10/20/11	Wallertech 39		7						He	4.00E-08								Ion beam profiles not current
10/22/11 10/29/11	Wallertech 39		7						He	4.00E-08								Ion beam current profiles
11/4/11 11/5/11	IQE 613858C	Cs	1	620	8.76	633	13.86	11.28	He	4.00E-08	1+8sec.	2	Negative	0.7	0.5	6	5	Standard dosing schedule
11/7/11 11/8/11	IQE 613858C	Cs	2	580	9.05	633	12.55	10.63	He	4.00E-08	1+9sec.	1	Negative	0.6 -		6	5	Standard dosing schedule
11/9/11	IQE 613858C		3						He	4.00E-08								Heat clean only, no activation
11/14/11 11/15/11	IQE 613858C	Cs	4	640	8.99	633	13.94	11.17	He	4.00E-08	1+9sec.	0.5	Negative	0.6	0.6	6	5	Standard dosing schedule
11/16/11 11/17/11	IQE 613858C	Cs+Li	5	670	9.03	633	14.53	13.56	He	4.00E-08	1+8sec.	2	Negative	0.9	0.6	6	5	Standard dosing schedule
11/18/11	IQE 613858C		6						He	4.00E-08								Heat clean only, no activation
11/21/11 11/22/11	IQE 613858C	Cs+Li	7	720	8.72	633	16.17	12.9	He	4.00E-08	1+9sec.	1	Negative	0.8	0.7	6	5	Standard dosing schedule
11/23/11 11/24/11	IQE 613858C	Cs+Li	8	670	9.47	633	13.86	1423	He	4.00E-08	1+9sec.	0.5	Negative	0.7	0.7	6	5	Standard dosing schedule
12/2/11 12/3/11	IQE 613858C	Cs	1	660	8.65	633	14.94		Kr	4.00E-08	1+9sec.	2	Negative	0.7	0.4	6	5	Standard dosing schedule
12/5/11 12/6/11	IQE 613858C	Cs	2	570	8.95	633	12.47		Kr	4.00E-08	1+9sec.	1	Negative	0.6	0.5	6	5	Standard dosing schedule
12/12/11 12/13/11	IQE 613858C	Cs	3	640	8.46	633	14.82	11.44	Kr	4.00E-08	1+9sec.	0.5	Negative	0.6	0.5	6	5	Standard dosing schedule
2/8/12 2/4/12	IQE 613858C	Cs+Li	1	430	8.4	633	10.03	16.07	Kr	4.00E-08	1+9sec.	2	Negative	0.9		6	5	Standard dosing schedule
2/7/12 2/8/12	IQE 613858C	Cs+Li	2	720	8.97	633	15.72	16.55	Kr	4.00E-08	1+8sec.	1	Negative	0.8	0.6	6	5	Standard dosing schedule
2/9/12 2/10/12	IQE 613858C	Cs+Li	3	730	8.55	633	16.72	14.65	Kr	4.00E-08	1+9sec.	0.5	Negative	0.6	0.5	6	5	Standard dosing schedule
2/13/12 2/14/12	IQE 613858C	Cs+Li	4	680	8.4	633	15.86	17.94	Kr	4.00E-08	1+9sec.	2	Negative	0.9	0.6	6	5	Standard dosing schedule
2/22/12 2/23/12	IQE 613858C	Cs	1	840	9.14	633	18	13.02	Ne	4.00E-08	1+9sec.	2	Negative	0.9	0.5	6	5	Standard dosing schedule
2/24/12	IQE 613858C	Cs	2	710	8.64	633	16.1	14.1										

2/28/12															
2/27/12	IQE 6135B/C	Cs	3	740	9.29	633	15.6	13.43	Ne	4.00E-08	1=9sec.	1 Negative	0.8	0.7	6	5	Standard cosing schedule
2/29/12																	
2/29/12	IQE 6135B/C	Cs	4	902	7.9	633	16.71	15.43	Ne	4.00E-08	1=9sec.	0.5 Negative	0.7	0.6	6	5	Standard cosing schedule
3/1/12																	
3/1/12	IQE 6135B/C	Ce+Li	4	902	7.9	633	16.71	15.43	Ne	4.00E-08	1=9sec.	2 Negative	1	0.7	6	5	Standard cosing schedule
3/2/12																	
3/2/12	IQE 6135B/C	Ce+Li	5	790	9.26	633	16.71	15.43	Ne	4.00E-08	1=9sec.	1 Negative	0.9	0.8	6	5	Standard cosing schedule
3/3/12																	
3/9/12	IQE 6135B/C		6			633			Ne	4.00E-08							Heat drain only, no ad sation
3/15/12	IQE 6135B/C	Ce+Li	7	790	9.75	633	15.87	15.13	Ne	4.00E-08	1=9sec.	0.5 Negative	0.8	0.8	6	5	Standard cosing schedule
3/16/12																	
4/10/12	IQE 6135B/C	Cs	1	670	8.47	633	15.49	12.23	Ar	4.00E-08	1=9sec.	2 Negative	0.9	0.5	6	5	Standard cosing schedule
4/11/12																	
4/12/12	IQE 6135B/C	Cs	2	660	8.37	633	15.45	11.97	Ar	4.00E-08	1=9sec.	1 Negative	0.7	0.5	6	5	Standard cosing schedule
4/13/12																	
4/16/12	IQE 6135B/C	Cs	3	670	8.75	633	15		Ar	4.00E-08	1=9sec.	0.5 Negative	0.6	0.5	6	5	Standard cosing schedule
4/17/12																	
4/18/12	IQE 6135B/C	Ce+Li	4	730	9.03	633	15.83	13.21	Ar	4.00E-08	1=9sec.	2 Negative	0.9	0.6	6	5	Standard cosing schedule
4/19/12																	
4/20/12	IQE 6135B/C	Ce+Li	5	640	8.62	633	14.94		Ar	4.00E-08	1=9sec.	1 Negative	0.8	0.6	6	5	Standard cosing schedule
4/21/12																	
4/23/12	IQE 6135B/C	Ce+Li	6	670	9.08	633	14.45	14.06	Ar	4.00E-08	1=9sec.	0.5 Negative	0.7	0.7	6	5	Standard cosing schedule

References

1. Y. Sun, R. E. Kirby, T. Maruyama, G. A. Mulhollan, J. C. Bierman and P. Pianetta, The Surface Activation Layer of GaAs Negative Electron Affinity Photocathode Activated by Cs, Li, and NF_3, *Appl. Phys. Lett.* **95,** 174109 (2009).

2. G. A. Mulhollan and J. C. Bierman, Photoyield Recovery of Cs+NF_3 Activated Negative Electron Affinity GaAs Photoemitters without additional Alkali Deposition, *J. Vac. Sci. B,* **28,** 899 (2010).

3. http://physics.nist.gov/PhysRefData/Handbook/Tables/xenontable1.htm.

4. H. C. Swart , J. S. Sebastian , T. A. Trottier , S. L. Jones , and P. H. Holloway, Degradation of Zinc sulfide Phosphors Under Electron Bombardment, *J. Vac. Sci. Technol. A* **14,** 1697 (1996).